

### **Author's Response:**

We thank both referees for acknowledging the significant changes done in the manuscript following their previous comments. We most appreciate the suggestion given in the scope of "minor changes" to better improve the manuscript. A point to point response to each referee is given below.

Sincerely,

Leenes Uzan, Dr. Smadar Egert and Prof. Pinhas Alpert

### **Authors' response to referee #1:**

#### **Referee comment:**

*Abstract: From the title one would expect that ceilometers provide the main contribution to the study. This is not reflected in the abstract anymore. Please highlight the role of ceilometers more clearly.*

**Author's response:** Comment accepted.

**Author's changes in manuscript:** We changed the title and the abstract accordingly.

#### **Referee comment:**

*Introduction: In general the authors followed the recommendations of the reviewers. However: check the "Stavros/Solomos"-problem (throughout the text; Stavros is the first name, so use Solomos!). Include a short section on the radiative forcing because this has now been covered in the results-section (as mentioned by reviewer #2 there are several papers in Tellus B special issues of 2009 and 2011). In my view the introduction is now sort of long. Certainly, the extension was triggered by trying to fulfill the requirements of review #2. Anyway, check if there is potential to slightly shorten it.*

**Author's response:** Comments accepted.

**Author's changes in manuscript:** Stavros was changed to Solomos. Reference to radiative heating was added to the "Results and discussion" section. The introduction was slightly shortened.

#### **Referee comment:**

*Ceilometer section: Include the statement of the limited measurement range more clearly – this was the major criticism of reviewer #2 (and also raised by me) – after (e.g.) line 286. This is indeed mandatory, and is independent on the problems discussed before (overlap, cosmetic shift, etc.): it is an effect of signal attenuation due to reduced atmospheric transmission and happens to all lidar systems (think*

about a dense cumulus cloud for example – the same effect). Thus, add 1-2 sentences here and refer to them later in the manuscript whenever necessary.

**Author's response:** Comments accepted.

**Author's changes in manuscript:** We added sentences referring to the limitations of ceilometers under dense conditions in the "ceilometers" subsection 2.1.

**Referee comment:**

*Ceilometer section: Line 246: Note that the statement in the Vaisala user's guide on the output does not fulfil strict scientific standards: "two-way attenuated backscatter profile with sensitivity normalized units (100000 srad km)<sup>-1</sup>" is not a physical quantity. These numbers are not the correct definition of attenuated backscatter (see  $\beta *$  in one of the cited Wiegner-papers and the explanations of reviewer #2) as it requires a calibration. Just state in the paper, that the range corrected signal (in arbitrary units) is stored (even this is not necessarily true if the h2-parameter is not set – this is fortunately not relevant for the lowest 2.4 km) and replace all cases of "attenuated backscatter". By the way: the authors correctly mentioned in line 264 that the "real" attenuated backscatter cannot be derived.*

**Author's response:** Comments accepted.

**Author's changes in manuscript:** We added the following text in "Ceilometers" subsection .2.1: "The internal calibration applied to convert the signal count output to "attenuated backscatter" does not always fully represent the actual lidar constant, therefore, it is not accurate enough for meteorological research. Hence, in this study we defined the ceilometer profiles as range corrected signal profiles in arbitrary units". We changed the "attenuated backscatter profiles" produced in this research to range corrected signal profiles (in a.u.).

**Referee comment:**

*Ceilometer section: Final comment (to lines 265ff, "Nevertheless..."): what is the purpose of these sentences: Rayleigh calibration is not possible, or Rayleigh requires averaging over 4 hours? Cloud calibration (see O'Connor et al., 2004) should be used? What is really meant with "background correction"?*

**Author's response:** Comments accepted.

**Author's changes in manuscript:** We changed the text to make it clearer.

**Referee comment:**

*Ceilometer section: Please reconsider my suggestions of the use of the (already listed) citations; they were not properly included. Ansmann et al. (2011) and Papayannis et al. (2008) are not covering ceilometers (but the benefit of lidars for dust observations in general), so these citations do not fit to lines 230–232 in V3. The statement on the water vapour absorption should be more precise (lines 276–278 of V3), maybe something like: "... water vapour distribution has a small effect on*

*the pronounced change of the signal shape at the top of the mixed layer or at boundaries of an elevated aerosol layer (Wiegner and Gasteiger, 2015)". The citation of Mona et al. (2012) is missing in the text.*

**Author's response:** Comments accepted.

**Author's changes in manuscript:** We relocated the citation and added the Mona et al. (2012) citation that was unfortunately neglected.

**Referee comment:**

*Results section: In context of Fig. 17 the authors refer to "attenuated backscatter". Either this should be changed to something like "range corrected signal with the Vaisala's inherent normalization" or better just "range corrected signal (in arbitrary units)". If the ceilometer's sensitivity remains constant during the event (which is likely) and the effect of changing water vapor absorption is neglected, even uncalibrated signals at a given site can be compared, i.e., discussion of the temporal evolution of the dust at that site is feasible and provides a useful contribution to the paper.*

**Author's response:** Comments accepted.

**Author's changes in manuscript:** The units in Fig. 17 were changed to range corrected signal profiles in a.u.

**Referee comment:**

*Results section: In view of the title of the paper I suggest to extend a little bit the discussion of the ceilometer data: As the MLH cannot be derived from the ceilometer data when the (strong) decrease of the transmission overcompensates the large backscatter coefficients of the dust, at least statements like "dust was present up to at least a height of xxx m" can be made. CALIOP data indicate that the top of the dust layer was typically between 2 and 4 km, however quite variable (in time and space) and sometimes multi-layered. Because of lack of co-located measurements (except the example shown in the revised paper, where some, but not all, ceilometer sites are met) no independent measurements of the actual distribution of the dust are available. Thus, the interpretation of the (upper part of the) ceilometer profiles must remain ambiguous. This can be discussed in the paper. However, when describing the lower boundary of the dust layer, the authors can rely on the ceilometer data (as they do in the revised version).*

**Author's response:** Comments accepted.

**Author's changes in manuscript:** The ceilometer contribution in the lower part of the atmosphere was better emphasized in the results section.

**Referee comment:**

*Results section: Line 571: What is meant with a "two-layer shape"? An elevated layer? Similar problem at line 618 ("arc shape ascent").*

**Author's response:** We referred to the ununiformed dust layer visible by the ceilometers' plots as two separate layers (descending down to 500 m ASL and rising from ground level). The "arc-shape" was referred to the thin dust layer formed aloft in the shoreline ceilometers following the entrance of the sea breeze front.

**Author's changes in manuscript:** We rephrased "two-layer shape" to "an ununiformed dust layer" and "arc-shape" to "a narrow dust layer".

**Referee comment:**

*Results section: Fig. 17: It seems that the height above sea level is shown, not the height above ground level as indicated by the y-axis. The figure caption seems to be okay.*

**Author's response:** Comment accepted.

**Author's changes in manuscript:** The y-axis was corrected height ASL.

**Referee comment:**

*Results section: Fig. 21: Give wavelength of the CALIOP-data. A blow-up is advisable to better see the situation over Israel. Comment on the "blue range" below 2 km: is this total attenuation? What is the elevation of the ground? What is the green line in the right panel showing?*

**Author's response:** We commented in line 627: "We assume the CALIOP lidar did not produce data beneath 2 km ASL due to total attenuation."

The green line indicates the overpass on 6 September 2015 referred by previous studies showing the distance from Israel. It is omitted in the updated CALIPSO plots.

**Author's changes in manuscript:** We focused the CALIPSO plots on the data produced above Israel. We addressed ground elevation height and mentioned the CALIOP wavelength (532 nm) in the caption of Fig. 21.

**Referee comment:**

*Conclusions: A general message to remember is missing: I suggest to clearly point out the contribution, the strengths, and the limitations of the ceilometer network when observing dust storms (not necessarily as strong as this event). In the paper they was demonstrated for one very strong event, but conclusions that are beneficial for future investigations and (maybe) can be used for other regions should be made.*

**Author's response:** Comments accepted.

**Author's changes in manuscript:** We have changed the conclusions section accordingly.

**Referee comment:**

*Miscellaneous: refer to Fig. 20 instead of Table 6 in line 355. Change "uncelebrated" to "uncalibrated" in line 281, captions of Figs. 6-13 should be changed to 7.-10. September.*

**Author's response:** Comments Accepted.

**Author's changes in manuscript:** Corrections were made accordingly.

**Author's' response to referee #2:**

**Referee comment:**

*P13, L355: Global radiation measured ... Table 6. .... ? In Table 6, I find PM10 for 31 stations only. Do you mean Table 7 (but I do not have Table 7?)*

**Author's response:** Mistake. The reference is Fig. 20

**Author's changes in manuscript:** The reference was changed from Table 6 to Fig. 20.

**Referee comment:**

*P13, L378: I have generally my problems with the uncertainty statements (here MSG, somewhere else MODIS). I think in the paper of Mamouri they compared MODIS with AERONET for these very large AODs and gave some uncertainty statements. At least, 15% uncertainty appears to me rather low... for these extreme dust conditions with AOD probably even larger than 3... , I think the AOD uncertainty is of the order of 1.0 or even more.*

*P14, L395: Again, an uncertainty of 0.1 is probably ok for AOD < 1.0, but what about cases with >2.5? Then the error is certainly much larger, of the order of 0.5 to 1.0.*

**Author's response:** We did not find explicit estimation of the MSG SEVIRI AOD uncertainty during high AOD values except for a general remark based on a comparison done between SEVIRI AOD and AERONET AOD in the scope of EUMETSAT Scientific Validation Report SEVIRI Aerosol Optical Depth (23 Oct 2017) : " For very high AOD conditions (>1.5) a negative bias is observed". Similar conclusions were found for MODIS AOD. We wish to thank Dr. Yevgeny Derimian from the university of Lille for data and personal correspondence on this issue.

**Author's changes in manuscript:** We added comments of increased uncertainty under high AODs (>1.5).

**Referee comment:**

*Section 3, I would introduce subsections! ... with head lines (titles): 3.1 7 September 2015, 3.2 8 September 2015 etc. That would make the full and very complex discussion section easier to read.*

*P15, L426: Now the ceilometer observations are introduced....*

**Author's response:** Comment accepted.

**Author's changes in manuscript:** We added subsection by dates as recommended.

**Referee comment:**

*P10, L286: you state: .... we refer to the ceilometer signal count profiles between 100-1000m. This statement is good, but I am afraid that non-lidar dust-interested readers will not remember that statement when they see Figures 6-12. I will come to this point again, below.*

*P23, L557: .. and now, the discussion of the 8 September starts. As mentioned above, we need a clear statement that the colored areas in Figs 6-12 only show the lowest few hundred meters of the dust layer (which actually reached up to 4-5 km according to all the articles published before: Mamouri, Solomos, Gasch, and all the CALIOP observations, including the one shown in Fig 21, and Fig.21 comes much too late, to my opinion). Without such a clear remark (and this remark is definitely not given), most readers will intuitively think, the ceilometers show the entire dust layer.*

*P24, L590: ... which may indicate the dust plume base height..... Again this statement is confusing when having the colored areas observed with ceilometers in mind, which suggest--- TOP HEIGHT. Non-lidar people will not understand what you want to say... without these explanations I suggested above.*

**Author's response:** The "Results and discussion" section is arranged by dates starting from 8 September 2015 to 10 September. The CALIOP observations refer to 10 September therefore they were mentioned last.

**Author's changes in manuscript:** We added a short paragraph in the "Results and discussion" section clarifying the colours of the ceilometers' plots in context of the ceilometers' measurement limitations.

**Referee comment:**

*If I compare Fig 9 with Fig 16 (the radiosonde profiles are very nice now!), then my opinion is confirmed that the ceilometers see only the lowest few hundred meters of the dust layer because the top height of the colored ceilometer backscatter areas coincide with the temperature inversion height (the base of the main dust layer, higher up...).*

**Author's response:** Agreed.

**Author's changes in manuscript:** No change.



**Referee comment:**

*Fig 13: This plots shows nothing? Clear skies? Or just overloaded by heavy dust? The plot is almost entirely deep blue! But there should be a lot of dust according to all the satellite observations presented. So, maybe an APD, PMT overloading effect. The ceilometer detectors were just overloaded because of the huge amount of dust around? Please clarify.*

**Author's response:** The deep blue scale evident in all Mount Meron ceilometer plots (Fig. 13) indicate total attenuation distinctively from 7 September ~ 14 UTC to 8 September ~ 16 UTC. Due to the complexity of the dust plume progress and the weak signal counts shown up to 3.5 km ASL (before 7 September ~ 14 UTC and after 8 September ~ 16 UTC), the assumption of a total attenuation throughout the period analysed is uncertain. Unfortunately, we did not have auxiliary measurements from the Mount Meron region to justify our assumptions.

**Author's changes in manuscript:** We added the aforementioned assumption in the manuscript.

**Referee comment:**

*Fig 17: Now the quantitative analysis is much improved. But I want to say, just that you think about it.....: An attenuated backscatter coefficient of  $10^{-4} \text{ m}^{-1} \text{ sr}^{-1}$  is equivalent to  $4 \text{ km}^{-1}$  extinction coefficient (for a lidar ratio of 40sr), and thus  $2 \times 10^{-4}$  means  $8 \text{ km}^{-1}$  extinction. Do you have the feeling, this is correct? I just ask you! Do you believe in your numbers?*

**Author's response:** Unfortunately Israel does not poses a calibrated lidar capable of true extinction measurements. However, previous study of the dust event in Cyprus by Raman lidar (Mamouri et al., 2016) provided extinction coefficient with similar order of magnitude. Based on the CL31 manual the ceilometer is capable to measure visibility values in clouds in the range of 15-150 m (dust visibility was estimation by IMS observers to be ~ 200 m) and hence, measurement capabilities within this range.

**Author's changes in manuscript:** No change.

**Referee comment:**

*The other point: Fig 17 nicely shows that backscatter signals (from five of the seven ceilometers) which are backscattered from heights above 500-700m were completely attenuated so that the attenuated backscatter coefficient is simply zero. That does not mean that the backscatter coefficient was zero..... The backscatter coefficient was probably even larger than at ground. So, attenuated backscatter is a very 'dangerous' parameter.*

**Author's response:** The attenuated backscatter profiles are the ones available from the ceilometers. Nevertheless, following the referees' recommendations and

changed the "attenuated backscatter" units to " range corrected signal profiles (in a.u.)".

**Author's changes in manuscript:** "Attenuated backscatter" units were changed to " range corrected signal profiles in a.u. ".

**Referee comment:**

*P23, L571: ... reveal a two-layer shape .... How do you know, there may have been even 4 or 5 distinct layers up to 4-5 km height.*

**Author's response:** We referred to the layers visible by the ceilometers (below ~ 1 km).

**Author's changes in manuscript:** We rephrased "two-layer shape" to " an ununiformed dust layer"

**Referee comment:**

*Fig.20: Black numbers on dark blue or dark brownish background... any idea to improve that?*

**Author's response:** Comment accepted.

**Author's changes in manuscript:** We changed the color of the numbers in figures 19-20 from black to white where the background was dark.

**Referee comment:**

*P26, L625: The dust top height of 2-4 km is mentioned here for the first time (if I read the paper carefully enough). This is simply much too late. And the overall context given by the papers of Mamouri et al., Solomos et al. (presenting CALIOP obs.), Gasch et al. (also presenting CALIOP obs.) clearly shows that the top height was always and everywhere at 4-5km height, in full agreement with your Fig 21 for 10 September. So, please improve.... Not 2-4 km, it was 4-5 km ...*

**Author's response:** Comments accepted.

**Author's changes in manuscript:** We rephrased the sentence to " ...a dust layer up to 5 km ASL".



## **A list of relevant changes made in the manuscript:**

1. Updated abstract
2. The introduction was shortened (Sect. 1)
3. The structure of "Results and discussion" section was changed.
4. The "Conclusions" section was broadened.
5. Several figures' presentation, unites and axis were changed.

1 **New insights into the vertical structure of the September 2015**  
2 **dust storm employing 8 ceilometers and auxiliary measurements**  
3 **over Israel**

4  
5 Leenes Uzan<sup>1,2</sup>, Smadar Egert<sup>1</sup>, Pinhas Alpert<sup>1</sup>

6  
7 <sup>1</sup>Department of Geosciences, Raymond and Beverly Sackler Faculty of Exact Sciences,  
8 Tel-Aviv University, Tel Aviv, 6997801, Israel.

9 <sup>2</sup>The Israeli Meteorological Service, Beit Dagan, Israel.

10  
11 Correspondence to: Leenes Uzan (Leenesu@gmail.com)

## 36 Abstract

37

38 On 7 September 2015 an unprecedented and unexceptional extreme dust storm struck the Eastern  
39 Mediterranean (EM) basin. Here, we provide an overview of the previous studies and describe the dust  
40 plume evolution over a relatively small area, i.e., Israel. This study ~~employs~~presents vertical profiles  
41 provided by an array of 8 ceilometers covering Israeli shore, inland and mountain regions. We employ  
42 multiple tools including ~~an array of eight ceilometers~~, spectral radiometers (AERONET), ground  
43 particulate matter concentrations, satellite images, global/diffuse/direct solar radiation measurements and  
44 radiosonde profiles. Main findings reveal that the dust plume penetrated Israel on the 7 September from  
45 the northeast in a downward motion to southwest. On 8 September, the lower level of the dust plume  
46 reached 200 m above ground level, generating aerosol optical depth ~~of (AOD>)~~ above 3, and extreme  
47 ground particulate matter ~~concentration measured on ground level~~concentrations up to  $\sim 10,000 \mu\text{m m}^{-3}$ .  
48 A most interesting feature on 8 September was the very high variability in the surface solar radiation in  
49 the range of 200-600  $\text{W m}^{-2}$  (22 sites) over just a distance of several hundred km in spite of the thick dust  
50 layer above. Furthermore, 8 September shows the lowest radiation levels for this event. On the following  
51 day, ~~9 September~~, the surface solar radiation increased, thus enabling a late ~~(between~~ 11-12 UTC) sea  
52 breeze development mainly in the coastal zone ~~along with 5 m s<sup>-1</sup> surface winds~~ associated with ~~are-~~  
53 ~~shaped~~ a creation of a narrow dust ~~layers.~~ layer detached from the ground. On 10 September the AOD  
54 values started to drop down to  $\sim 1.5$ , the surface concentrations of particulate matter decreased as well  
55 as the ceilometers aerosol indications; ~~Still, as indicated by (signal counts) although~~ CALIPSO ~~a 2-4~~  
56 ~~km~~ revealed an upper dust layer remained.

57

58

59

60

61

62

63

64

65

66

67

68

69

# 70 1. Introduction

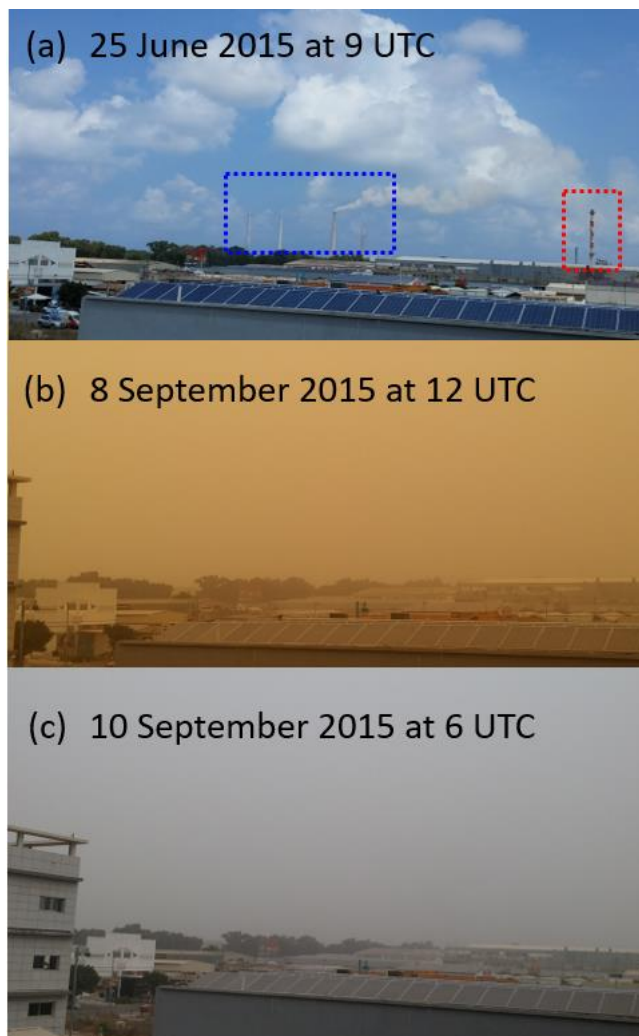
71

72 An exceptionally extreme dust storm prevailed over the Eastern Mediterranean (EM) on September  
73 2015. The Israeli meteorological service (IMS) declared the dust storm to be extraordinary as it occurred  
74 on early September (7-10 September), extended over a time span of 100 hours creating extreme ground  
75 level particulate matter (PM) concentrations (e.g. 100 times above the hourly average of PM10 in  
76 Jerusalem). On 7 September, prior to the penetration of the dust storm over Israel, IMS reported  
77 (<http://www.ims.gov.il/IMS/CLIMATE>; (<http://www.ims.gov.il/IMS/CLIMATE>; in Hebrew) a heat  
78 wave ~~which prevailed~~ over Israel causing harsh weather conditions of 80-90% relative humidity, 42 °C  
79 in valleys, 38 °C in mountains. On 8 September, visibility decreased below 3 km and consequently, inland  
80 aviation was prohibited until ~~the~~ 9 September (Fig.1). Concurrently, severe ground level PM  
81 concentrations resulted with a public warning from outdoor activities; issued by the environmental  
82 protection ministry. Finally, on 11 September, as visibility increased, the IMS confirmed the dust storm  
83 ended, whereas the heat wave was over ~~only~~ two days later, on 13 September, subsequent to a profound  
84 change in weather conditions. The PM concentrations declined to values measured prior to the dust  
85 storm (<http://www.svivaqgm.net/Default.rtl.aspx>; (<http://www.svivaqgm.net/Default.rtl.aspx>; in Hebrew)  
86 only on 14 September, though the AERONET measurements (<https://aeronet.gsfc.nasa.gov>) stationed in  
87 central and southern Israel reveal that the aerosol optical depth (AOD) resumed to values prior to the dust  
88 storm only on 17 September.

89

90

91



92  
 93 Figure 1. Photographs taken from the central coast of Israel, adjacent to the Hadera ceilometer, 3.5  
 94 km southeast to ~~the~~ stacks of a power plant (indicated by a blue rectangle) and 600 m north to a  
 95 factory stack (indicated by a red rectangle). The photographs were taken prior to the dust storm, on  
 96 25 July 2015 (a)), and during the dust storm, on 8 September 2015 (b) and 10 September 2015 (c).  
 97 Notice that ~~during the dust event (b,e)~~ the stacks ~~clearly seen in (that are visible on a) from the same~~  
 98 ~~spot, clear day (a)~~ are invisible. ~~during the dust storm (b, c).~~

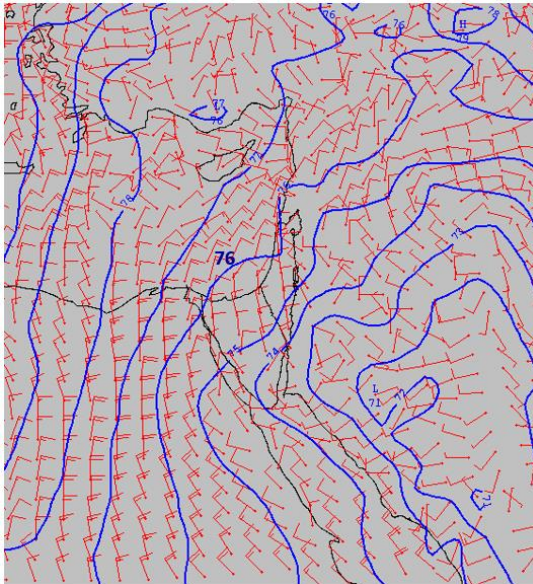
99  
 100 Investigation of the mechanisms leading the severe dust storm was performed by Gasch et al. (2017)  
 101 using a state of the art dust transport model ICOSahedral Nonhydrostatic (ICON) with the Aerosol and  
 102 Reactive Trace gases (ART) (Rieger, et al., 2015). The model concentrated on the EM with one global  
 103 domain (40 km grid spacing, and 90 vertical levels from 20 m to 75 km) and 4 nested grids (20, 10, 5  
 104 and 2.5 km grid spacing and 60 vertical levels from 20 m to 22.5 km). Simulations were done for three  
 105 consecutive days from 6-8 September. Model results delineated an unusual early incidence of an active  
 106 Red Sea Trough (Fig.2; Alpert et al, 2004) over Mesopotamia, followed by meso-scale convective  
 107 systems over the Syrian-Iraqi border generating three cold-pool outflows. On the night between 5 and 6

108 September, a convective system fueled by an inflow along the eastern side of the Red Sea Trough, moved  
109 northeast over the Turkish-Syrian border region. The convective system intensified overnight and  
110 generated a first weak cold pool outflow on ~~the~~ 6 September. After sun rise, ~~as the nocturnal boundary~~  
111 ~~layer dissipated, an increase of downward mixing lead to~~ an increase of surface wind speeds ~~consequently~~  
112 ~~causing~~caused dust ~~to~~ pick up over Syria. ~~The high surface wind speeds sustained during the day due to~~  
113 ~~a strong and shallow heat low whereas sea breeze transported dust to the south towards Jordan. At this~~  
114 ~~point, the~~The atmospheric instability over the Syrian-Iraqi border created a second convective ~~cool~~cold  
115 ~~pool~~ pool outflow from the Zagros mountain range west into Syria. The gust from the second ~~cool~~cold  
116 outflow ignited a third ~~cool~~cold pool outflow at 20 UTC. ~~The third outflow which~~ moved southerly along  
117 the eastern flank of the Red Sea Trough ~~and shifted warm and moist air masses along the way. Past~~  
118 ~~midnight, on. On~~ 7 September, ~~the intensified third cool pool outflow shifted to the west. At 10 UTC~~7  
119 ~~September,~~ rainfall and an increase of surface wind speeds north-west of Syria strengthened the third  
120 ~~cool~~cold pool outflow. ~~Consequently, leading to transportation of~~ enormous dust emissions  
121 ~~transported (up to 5 km) southwest up to 5 km. The. By nightfall of 7 September, the~~ aged second ~~cool~~cold  
122 pool ~~outbreak re-intensified~~outflow merged with the third cold pool outflow, over Jordan and  
123 southwestern Syria ~~and merged with the third outflow with the nightfall of 7 September.~~ After midnight,  
124 ~~on~~between 7 and 8 September, the dust transported over Israel ~~and was mostly influenced by local~~  
125 ~~circulation systems in the EM.~~ Model simulations were compared to in-situ measurements and satellite  
126 images: visible electromagnetic spectrum from Moderate Resolution Imaging Spectroradiometer  
127 (MODIS: <https://modis.gsfc.nasa.gov/>) aboard the Aqua satellite; AOD from the Terra satellite; RGB  
128 dust product from the Spinning Enhanced Visible and InfraRed Imager (SEVIRI) upon the Meteosat  
129 Second Generation (MSG) satellite; ~~total~~Total attenuated backscatter from Cloud-Aerosol Lidar upon  
130 the Infrared Pathfinder Satellite Observations (CALIPSO: <https://www-calipso.larc.nasa.gov/>).  
131 ~~Ground~~Investigation over Israel employed measurements from ground level meteorological  
132 ~~measurements~~stations (3 sites) and PM ~~concentration~~measurements (3 sites) ~~in Israel were employed.~~  
133 Results revealed the model lacked sufficient development of a super critical flow, which in effect  
134 produced the excessive surface wind speeds. Eventually, this misled the forecast of the dust advection  
135 southwest into Israel.

136

137





138

139

140

141

142

143

144

145

146

147

148

149

150

151

152

153

154

155

156

157

158

159

160

161

Figure 2. 925 mb map from 7 September 2015 12 UTC of ~~the~~ geopotential height ~~with~~of 1 dm interval (blue lines, the 76 dm line ~~is~~ passing over Israel; ~~blue lines~~) and wind (~~red arrows~~, 10 KT each line; ~~red arrows~~). Source: IMS from UKMO British Met Office model.

The fact that forecast models did not succeed in predicting this outstanding dust event motivated Mamouri et al. (2016) to study its origin and development. Their research presented dust load observations in the Cyprus region. Luckily, at the time of the dust storm, an EARLINET (European Aerosol Research lidar Network: <https://www.earlinet.org/>) Raman lidar stationed in Limassol provided vertical dust profiles and valuable optical dust properties of backscatter, extinction, lidar ratio and linear depolarization ratio. They analyzed the optical thickness (AOT) and Angström exponent derived from the MODIS Aqua satellite. MODIS Aqua AOT measurements were compared to the Limassol lidar observations, AOD measurements from two AERONET sites (Cyprus and Israel) and ground level PM10 concentration from four Cyprus sites. On 7 September, EARLINET lidar observations measured two dust layers (extending up to 1.7 km ASL and between 1.7-3.5 km ASL). The dust particle extinction coefficient measured in Limassol had reached  $1000 \text{ Mm}^{-1}$  followed by high PM10 concentration of  $2000 \mu\text{m m}^{-3}$ . -Extreme values over Limassol, were reported on ~~the~~ 8 September as MODIS Aqua AOT observations exceeded 5 (assuming overestimation up to 1.5) and hourly PM10 concentration of about  $8,000 \mu\text{m m}^{-3}$  (with uncertainties in the order of 50%). Unfortunately, on ~~the~~ 8 September, the lidar was intentionally shut down to avoid potential damage to the instrument. ~~Nevertheless, -lidar~~ Lidar observations indicated another dense dust outbreak (1-3 km ASL) reaching Limassol on ~~the~~ 10 September, also visible by ~~the~~ AOT MODIS Aqua ~~AOT imagery~~. The researchers concluded the scale of the dust storm features was too small for global and regional dust transport models. They presumed that

162 the initiation of the dust plume was due to an intense dust storm (~~Habbe~~haboob) in northeastern Syria  
163 and northern Iraq, leading to vigorous downbursts which consequently pushed huge amounts of dust and  
164 sand to the atmosphere. The lidar observations indicated a double layer structure of the dust, 1.5 and 4  
165 km ~~above sea level~~(ASL),<sub>2</sub> pointing to multiple dust sources.

166  
167 Stavros Solomos et al., (2016) continued the investigation of the formation and mechanism of the dust  
168 storm over Cyprus by a high regional atmospheric model of the integrated community limited area  
169 modeling system (RAMS-ICLAMS). The model simulations focused on the generation of the dust storm  
170 on 6 and 7 September. Model results were fine-tuned by observations from EARLINET lidar stationed  
171 in Limassol, radiosonde data from five sites (Cyprus, Israel, Jordan, and two from Turkey) and satellite  
172 imagery from MSG SEVIRI and CALIPSO CALIOP. The model was set to three grid space domains:  
173 an external grid of 12X12 km, (over the EM) an inner set at 4X4 km (over northern EM) and 2X2 km  
174 grid for cloud resolving (over northeastern Syria). The vertical structure consisted of 50 terrain following  
175 levels up to 18 km. The researchers ~~assessed~~estimated a strong thermal low over Syria was followed by  
176 convection activity over the Iraq-Iran-Syria-Turkey borderline ~~combined~~. Combined with land use  
177 changes (aftermath of the war held in Syria~~), these conditions~~ manufactured the extreme dust storm. The  
178 model succeeded to describe the dust westward flow of a haboob containing the dust previously elevated  
179 over Syria as also observed by MSG SEVIRI and EARLINET lidar. However, there were some  
180 inaccuracies in the quantification of dust mass profiles. ~~They~~The researchers attributed the model  
181 discrepancies to the limited ability of the model to properly resolve dust and atmospheric properties (e.g.  
182 change of land use and intense downward mixing).

183  
184 ~~Evaluation whether the dust activation due to human perturbations to land use (such as in the~~  
185 ~~Syria civil war) had an underlying effect on the dust storm formation or even to its increase were studied~~  
186 ~~by~~ Pu and Ginoux, (2016). ~~They~~ examined the connection between the natural climate variability (the  
187 Pacific decadal oscillation) and the dust optical depth (DOD) in Syria. ~~DOD, between the years 2003-~~  
188 2015. DODs were derived by the deep blue algorithm (Hsu et al., 2013) aerosol product from MODIS  
189 Terra and MODIS Aqua satellite (10 km resolution ~~picture~~) ~~was combined with monthly horizontal winds~~  
190 ~~and geopotential heights generated~~. AODs were estimated by the European Centre for Medium-Range  
191 Weather Forecasts (ECMWF) reanalysis model (horizontal resolution of 80 km and 37 vertical levels).  
192 ~~The dataset of DODs during the years 2003-2015 were compared to) and produced by~~ the Geophysical  
193 Fluid Dynamics Laboratory (GFDL) Atmospheric model (AM3) (Donner et al., 2011). ~~The~~In addition,  
194 the AM3 model produced ~~AODs and calculated the~~ mass distribution and optical properties of aerosols,  
195 their chemical production, transport, and dry or wet deposition. Comparison of AODthe model results,

196 ~~AOD~~AODs, AERONET AOD measurements and ~~DOD~~DODs from satellite observations revealed the  
197 model underestimated the ~~AOD's~~AODs particularly in the EM. The authors assumed that the soil  
198 moisture parameter in the model were not set properly resulting in the AOD dissimilarities.

199  
200 The impact of the conflict in Syria on the aridity of the region and therefore, a possible direct  
201 impact on the generation of the September dust storm was examined by Parolari et al., (2016). The  
202 researchers conducted simulations using the Advanced Research Weather Research and Forecasting  
203 (WRF-ARW) model from 30 August 2015 to 10 September 2015 over the EM. The model consisted of  
204 two nested domains (9 and 3 km grid spacing and 35 vertical levels). Daily and monthly AOD data from  
205 MODIS were computed by the deep blue algorithm over land. ~~Anomalies of the September 2015 monthly~~  
206 ~~average AOD were compared to the monthly average of 2000-2015.~~ The monthly average of September  
207 2015 vegetation status in the region was estimated by MODIS normalized difference vegetation index  
208 (NDVI). Historical data was divided into two periods: none-drought (2001-2006) and drought (2007-  
209 2010). Wind shear stress was calculated to estimate wind erosion. ~~Their~~Main findings reveal that the  
210 enhanced dust uplift and transportation of the September 2015 dust storm was due to meteorological  
211 conditions rather than the land-use changes ~~because of~~attributed to the civil conflict in Syria. WRF  
212 simulations revealed ~~the well known Shamal winds and cyclone associated with dust storms in the~~  
213 ~~Middle East (Rao et al., 2003) were characterized by~~ northwesterly winds west of the low pressure zone  
214 in the Syrian-Iraqi border. ~~However, the~~ were associated with dust storms in the Middle East (Rao et al.,  
215 2003). The source of elevated dust concentrations over the EM coast on ~~the 7 and~~ 7 and 8 September were  
216 attributed to the cyclone front movement. On 6 September low level winds (700 hPa) were opposite to  
217 the northwesterly high level winds (300 hPa) ~~winds,~~ consequently, generating enhanced surface shear  
218 stress and transported re-suspended PM westward. Furthermore, based on the past 20 years, the Israeli  
219 summer of 2015 was unusually dry and hot and therefore enabled easier updraft of dust soil increasing  
220 the probability of dust emissions.

221  
222 Jasmin (2016) compared the dust storm plume aerosol content provided by MSG SEVIRI  
223 observations, to the ~~results~~generation of the dust storm produced by the open source Meteoinfo model  
224 (Wang, 2014). The Meteoinfo model was based on meteorological variables from ECMWF. The model  
225 ~~meteorological conditions suggested~~revealed a formation of two simultaneous dust storms, from northern  
226 Syria and ~~from~~ the Egyptian Sinai desert, ~~resulting from~~ as a result of updrafts created by low pressure  
227 systems.

228

229 \_\_\_\_\_ The aforementioned studies (summarized in Table 1) focused on the generation of the dust storm  
230 in the Syria region based on transport models, satellite imagery and in situ measurements. In our study  
231 we focus on the evolution of the dust plume over Israel in the lower atmosphere based on an array of 8  
232 ceilometers, ~~52 in situ PM measurements, two AERONET sites and satellite imagery. We do not~~  
233 ~~investigate the reasons of the models frailer to predict this extraordinary storm, but rather attempt to~~  
234 ~~present details of the evolution of the dust plume passage over Israel. The data presented here can be~~  
235 ~~used as a tool to verify state of the art model simulations and provide a different point of view to the~~  
236 ~~meteorological conditions governing the dust plume advection over the EM.~~

237  
238 ~~In the following section we describe the measuring sites and instruments in this study. and auxiliary~~  
239 ~~instruments described in Sect. 2.~~ The list of instruments includes; ceilometers, PM measurements,  
240 AERONET, radiosonde, solar radiation and satellite imagery. Sect. 3 presents the ~~results~~delineation of  
241 the dust plume spatial and temporal scheme ~~delineated by the ceilometer plots on~~from 7 September  
242 ~~through the~~ 10 September 2015. We discuss and compare the results between the ~~ceilometer plots and~~  
243 ~~the aforementioned auxiliary~~different measurements. ~~In Sect. 4 we conclude our~~ Conclusions and main  
244 findings of the dust plume advection progress in the lower atmosphere ~~above Israel and the downward~~  
245 ~~transport towards the ground.~~are given in Sect. 4.

## 248 2. Instruments

### 249 2.1 Ceilometers

251  
252 Lidars are widely used for aerosol studies (Ansmann et al., 2011; Papayannis et al., 2008) including  
253 desert dust characteristics and transport process (Mona et al., 2012). Ceilometers, initially intended for  
254 cloud level height detection, are automatic low cost lidars widespread in airports and weather stations  
255 worldwide. As single wavelength lidars, ceilometers cannot produce the information aerosol properties  
256 such as size distribution, scattering and absorption coefficients. ~~(Ansmann et al., 2011; Papayannis et al.,~~  
257 ~~2008).~~ Nevertheless, with improvement of hardware and firmware over the years, ceilometers have  
258 become a valuable tool in the study of the atmospheric boundary layer and the vertical distribution of  
259 aerosols layers (Haeffelin and Angelini, 2012; Ansmann et al., 2003). Furthermore, in 2013 ceilometers  
260 ~~been~~were assimilated in the EUMETNET (European Meteorological Services network) Profiling  
261 Program ~~—(Eprofiling program across Europe (http://eumetnet.eu/activities/observations-~~

programme/current-activities/e-profile) to develop a homogeneous dataset from automatic lidars and state-of-the-art Vaisala ceilometers across Europe ([http://eumetnet.eu/activities/observations\\_programme/current-activities/e-profile/alc-network/](http://eumetnet.eu/activities/observations_programme/current-activities/e-profile/alc-network/)). CL31, commonly deployed worldwide.

Vaisala ceilometers type CL31, are commonly deployed worldwide, and the main research tool in this study as well. CL31 is a pulsed elastic micro lidar, employing an Indium Gallium Arsenide (InGaAs) laser diode transmitter of near infrared wavelength of (910 nm  $\pm$  10 nm at 25°C). In order to compensate the low pulse energy of the laser (hence defined "eye-safe") and to provide sufficient signal to noise ratio, the pulse repetition rate is of 10 kHz every two seconds (Vaisala ceilometer CL31 user's guide: <http://www.vaisala.com>). The backscatter signals are collected by an avalanche photodiode (APD) receiver and designed into attenuated backscatter range corrected signal profiles within a reporting interval of 2-120 s (determined by the user) given in relative units (signal counts). The attenuated backscatter ceilometer profiles are automatically corrected by an internal calibration (resulting in a multiplication factor of  $10^{-8}$  to convert the signal count to attenuated backscatter), a cosmetic shift of the backscatter signal (to better visualize the clouds base), an obstruction correction (when the ceilometers' window is blocked by a local obstacle) and an overlap correction (to the height where the receiver field of view reaches complete overlap with the emitted laser beam).

Vaisala provides a scaling factor transferring signal counts to attenuated backscatter units by a multiplication factor of  $10^{-8}$ . The scaling factor was obtained using a calibration procedure operated on a several instruments and cross-checked by signal integral from water clouds. The uncertainty of calibrated attenuated backscatter profile (with a 100% clean window condition) was of  $\pm 10\%$ . The uncertainty for the estimated attenuated backscatter was of  $\pm 20\%$  (Münkel C., private communication). However, Kotthaus et al., (2016) emphasize that this internal calibration applied to convert the signal count output to attenuated backscatter units does not always fully represent the actual lidar constant, therefore, it is not accurate enough for meteorological research. Hence, in this study we defined the ceilometer profiles as range corrected signal profiles in arbitrary units.

Kotthaus et al., (2016) examined the Vaisala CL31 ceilometer by comparing the attenuated backscatter profiles from 5 units with different specification of sensor hardware, firmware and operation settings (noise, height and time reporting interval). Research findings show the instrument characteristics that affect the quality and availability of the attenuated backscatter profiles in the following manner are as follows: At high altitudes, a discontinuity in the attenuated backscatter



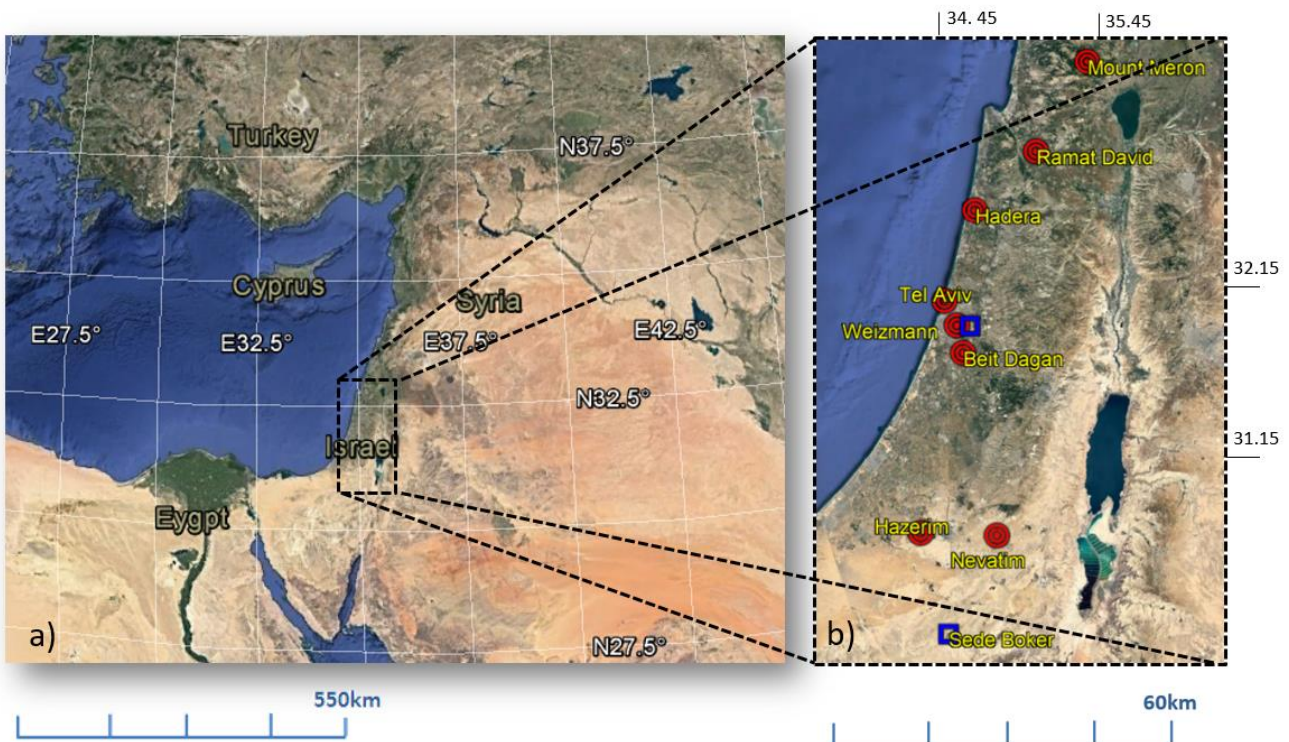
296 profile is evident at two height points, ~ 4949 and 7000 m. Background signals (instrument related) and  
297 cosmetic shift (firmware dependent) tend to be either negative or positive up to 6000m and then switch  
298 signs above ~ 6000 m. Below 70 m an overlap correction is applied internally by the ceilometer sensor  
299 as well as an obstruction correction (below 50 m). Between 50-80 m hardware related perturbation cause  
300 a slight offset in the attenuated backscatter values. The authors advise the user-defined reporting interval  
301 should be no shorter than 30s to avoid consecutive profiles partial overlap. However, they emphasize the  
302 internal calibration applied to convert the signal count output to “attenuated backscatter” does not always  
303 fully represent the actual lidar constant, therefore, it is not accurate enough for meteorological research.  
304 Nevertheless, since ceilometers are not sensitive to molecular scattering and solar radiation contributes  
305 to the random noise, a background correction can be derived by a 4 hr round of midnight attenuated  
306 backscatter profiles. Furthermore, aBackground noise reduction can be achieved by a procedure based  
307 on long averaging period at nighttime during a clear atmosphere. A range corrected attenuated backscatter  
308 can be derived by the attenuated backscatter profiles during an existence of a stratocumulus cloud.

309  
310 ~~—Furthermore,~~Weigner et al, (2014) studied different retrieval methods to derive the aerosol  
311 backscatter coefficient from the ceilometers' attenuated backscatter profiles based on a comparison to  
312 auxiliary collocated instruments such as a ~~sunphotometer~~Sunphotometer or a multiwavelength lidar. They  
313 focused on calibration methods, the range detection limitations by the overlap function and the sensitivity  
314 of the attenuated backscatter signal to relative humidity. Although, the ceilometer wavelength range  
315 (given as  $905 \pm 3$  nm) is influenced by water ~~vapour~~vapor absorption, in the case of aerosol layer  
316 detection, water ~~vapour~~vapor distribution has a small effect on the signal change, indicating the mixed  
317 layer height (MLH) or an elevated mixed layer, as the aerosol backscatter itself remains unchanged.  
318 (Wiegner and Gasteiger, 2015). Consequently, except for a case of a dry layer in a humid MLH, ~~the~~water  
319 ~~vapour~~vapor is unlikely to lead misinterpretation of the aerosol stratification. Fortunately, most  
320 algorithms are based on a significant signal slope to define the aerosol layers, therefore, can be  
321 determined from ~~uncelebrated~~uncalibrated ceilometer attenuated backscatter profiles. ~~The wavelet~~  
322 ~~covariance transform (WCT) was the method used in this study to evaluated the MLH (Uzan, et al, 2016),~~  
323 ~~whether determined by the creation of thermals or the subsidence of the dust plume.~~

324  
325 ~~—In this study, we address the aforementioned limitations as we refer to the ceilometer signal~~  
326 ~~count profiles between 100–1000 m AGL. The~~In this research, ceilometer array is comprised of 8 units  
327 in different sites (Fig 3 and Tables 2-3), 6 of which are owned by a governmental office. The ceilometers  
328 are CL31 type apart for ceilometer CL51 stationed in the Weizmann Institute which has a higher  
329 backscatter profile range (up to 15.4 km, Munkel et al., 2011). Unfortunately, calibration procedures



330 were not held and maintenance (cleaning of the ceilometer window) was done regularly only ~~for~~<sup>in</sup> the  
 331 Beit Dagan ceilometer. Apart from the Beit Dagan and Weizmann ceilometers (~~Table 4~~), we could not  
 332 retrieve the technical information of firmware and hardware type- (~~Table 4~~). However, we have been  
 333 confirmed (personal communication) that the combination of hardware and firmware had been done  
 334 following Kotthaus et al (2016). The Beit Dagan ceilometer signal count were found to be weaker (up to  
 335 800 signal count compared to 10,000 in the other CL31 ceilometers) due to different hardware definitions.  
 336 Therefore, in order to present the Beit Dagan attenuated backscatter range corrected signal profiles  
 337 aligned with the profiles of the other ceilometers (given in Fig. 17), the Beit Dagan attenuated  
 338 backscatter range corrected signal values were multiplied by 12.5 (10,000/800). We address the  
 339 mentioned limitations of the ceilometers measurements in the first range gates as we refer to the  
 340 ceilometer signal count from 100 m AGL. Due to the extreme AOD values of the September dust storm,  
 341 high extinction of the ceilometer signal limited the height of profile analyzed down to 1000 m AGL.



344  
 345 Figure 3. Google Earth map of the large domain (a) and Israel (b) with indications of 8 ceilometer  
 346 sites (red circle; detail in Table 2) and two AERONET sites (blue square).

347  
 348  
 349  
 350

## 2.2 Radiosonde

Radiosonde (RS) type Vaisala RS41-SG is launched by the IMS twice a day at 00 UTC and 12 UTC from the Beit Dagan site adjacent to the Beit Dagan ceilometer. The radiosonde produces profiles of humidity, temperature, pressure, ~~and~~ wind speed and wind direction. The output files were downloaded from the University of Wyoming site (<http://weather.uwyo.edu/upperair/sounding.html>, station number 40172). With respect to Stull (1988), the MLH was defined by the RS profiles as the height where ~~the following phenomena were identified~~; was identified along with a significant drop in ~~the~~ relative humidity, strong wind shear and an increase in the virtual temperature (Uzan et al., 2016; Levi et al., 2011).

## 2.3 Particulate matter monitors (PM10, PM2.5)

PM monitors are low-volume flow rate Thermo Fisher Scientific type FH 62 C14 (beta attenuation method) and type 1405 TEOM (Tapered Element Oscillating Microbalance method). Both instruments report PM concentration every 5 min. The location of PM measurement sites is given in Tables 5. In the beta attenuation method (<https://www3.epa.gov/ttnamti1/files/ambient/inorganic/overvw1.pdf>) (<https://www3.epa.gov/ttnamti1/files/ambient/inorganic/overvw1.pdf>) low-energy beta rays are focused on deposits on a filter tape and attenuated according to the approximate exponential function of particulate mass (i.e., Beer's Law). These automated samples employ a continuous filter tape. The attenuation is measured through an unexposed portion of the filter tape ~~is measured, the~~. The tape is then exposed to the ambient sample flow where a deposit is accumulated. The beta attenuation is repeated, and the difference in attenuation between the blank filter and the deposit is a measure of the accumulated concentration. The weighing principle used in the TEOM method (<https://tools.thermofisher.com/content/sfs/manuals/EPM-TEOM1405-Manual.pdf>) (<https://tools.thermofisher.com/content/sfs/manuals/EPM-TEOM1405-Manual.pdf>) is based on a mass change detected by the sensor as a result of the measurement of a change in frequency. The tapered element at the heart of the mass detection system is a hollow tube, clamped on one end and free to oscillate at the other. If additional mass is added, the frequency of the oscillation decreases ~~– and~~ a precision electronic counter measures the oscillation frequency with a 10-second sampling period. An electronic control circuit senses oscillation and adds sufficient energy to the system to overcome ~~losses.~~ Losses while an automatic gain control circuit maintains the oscillation at a constant amplitude. A

384 ~~precision electronic counter measures the oscillation frequency with a 10-second sampling period. Both~~  
385 ~~instruments report PM concentration every 5 min. The location of PM measurement sites is given in~~  
386 ~~Tables 5.~~

387  
388

## 389 2.4 AERONET

390

391 AEROSOL ROBOTIC NETWORK (AERONET) is multiband photometer with an automatic sun tracking  
392 radiometer for direct sun measurements with a spectral range of 340 ~~to~~ 1640 nm wavelengths. The  
393 photometer measures the solar extinction in each wavelength to compute aerosol optical depth (Holben  
394 et al., 1998). In Israel ~~two~~, AERONET units type CE318-N (<https://aeronet.gsfc.nasa.gov>) operate in  
395 Sede Boker and the Weizmann Institute (Fig. 3). Unfortunately, the unit in Weizmann did not operate  
396 ~~duringbetween~~ 6-8 September 2015 due to power failure. ~~InFor~~ this study ~~we used~~, data acquisition was  
397 comprised of AOD (500 nm wavelength) and Ångstrom exponent (440-870 nm wavelengths) based on  
398 AERONET Level 2.0 data (cloud screened and quality assured for instrument calibration) for AOD at  
399 500 nm and the Ångstrom Exponent defined by 440-870 nm.

400  
401

## 402 2.5 Global, direct and diffuse solar radiation measurements

403

404 Global solar radiation is measured ~~in~~ by ~~IMS in 22 sites (Table. 6) by instrument type~~ Kipp & Zonen  
405 pyranometer ~~CMP-11. Integrated solar radiation type CMP-11 in 22 sites (Fig. 20) operated by the IMS.~~  
406 The pyranometer produces 10 min measurements of the integrated radiation flux (W m<sup>-2</sup>) ~~frombetween~~  
407 300 ~~to~~ 3000 nm ~~is produced every 10 min. wavelengths.~~ Diffuse and direct radiation are also measured  
408 in Beit Dagan (coastal region, 31 m ASL) and Beer Sheva (southern region, 71 m ASL). For diffuse  
409 radiation measurements, a ring is installedmounted over ~~thea~~ pyranometer to shadeavoid direct solar  
410 radiation. Direct radiation is measured by a sun tracker pyrheliometer.

411  
412

413  
414

415  
416

## 2.6 Satellite imagery

### 2.6.1 SEVIRI (MSG satellite)

Meteosat Second Generation (MSG) is a new series of European geostationary satellites operated by EUMETSAT (European Organization for the Exploitation of Meteorological Satellites). On board the MSG is a 12-channel Spinning Enhanced Visible and Infrared Imager (SEVIRI) (Roebeling et al., 2006). The combination of red, blue and green (RGB) channels (12-10.8  $\mu\text{m}$ , green:10.8-8.7  $\mu\text{m}$ , blue:10.8  $\mu\text{m}$ , respectively) produce imagery of dust in pink or ~~magenta~~magenta, dry land in pale blue at daytime and pale green at nighttime, ~~thick~~. Thick high-level clouds in red-brown tones and thin high-level clouds appear nearly black (~~<http://oiswww.eumetsat.int/>~~)(<http://oiswww.eumetsat.int/>). Access to EUMETSAT imagery is ~~given~~ in ~~<https://www.eumetsat.int/website/home/Images/RealTimeImages/index.html>~~ provided online by ~~<https://www.eumetsat.int/website/home/Images/RealTimeImages/index.html>~~. Several studies compared AOD from MGS SEVIRI and AERONET measurements (Romano et al., 2013; Bennouna et al., 2009; Jolivet et al., 2008) ~~compared AOD from MGS SEVIRI and AERONET measurements clarified~~showed the uncertainty of MSG SEVIRI AOD decreases as AOD rises. For continental aerosol type, errors do not exceed 10 % in viewing zenith angles between 20° and 50°, ~~probable for the study area considered here~~. ~~Overall, the~~. The MSG SEVIRI AOD uncertainty it is expected to be under 15% (Mei et al, 2012) and even higher as the atmospheric AOD increases above 1.5 (EUMETSAT Scientific Validation Report SEVIRI Aerosol Optical Depth (23 Oct 2017)). North Africa Sand storm survey (NASCube: <http://nascube.univ-lille1.fr>) obtains AOD by temperature anomalies ~~of~~based on SEVIRI RGB by evaluating the difference in the emissivity of dust and desert surfaces during daytime.

### 2.6.2 MODIS (Terra and Aqua satellites)

The MODERate resolution Imaging Spectrometer (MODIS) instrument ~~flies~~is stationed aboard the Earth Observation System's (EOS) Terra and Aqua polar-orbiting satellites, ~~with~~. Terra satellite is on a descending orbit (southward) over the equator ~~about~~at ~ 10:30 local sun time, ~~and~~. The Aqua satellite is on an ascending orbit (northward) over the equator ~~about~~at ~ 13:30 local sun time. MODIS performs measurements by 36 channels between 412 ~~to~~-14200 nm whereas the aerosol retrieval makes use of seven channels (646, 855, 466, 553, 1243, 1632 and 2119 nm central wavelength), ~~and~~ together with a

450 number of other wavelength bands ~~associated with for~~ screening procedures. ~~Remer et al., As land signals~~  
451 ~~(AERONET) and the atmospheric signals are comparable at ~550 nm,(2006) revealed~~ errors of 0.01 in  
452 ~~assumed the MODIS~~ surface reflectance will lead to errors on the order of 0.1 in AOD retrieval ~~).~~  
453 ~~However, under conditions of high AOD (<1.5) the uncertainty is expected to rise. Remer et al., 2006).~~

454

455

### 456 **2.6.3 CALIOP (CALIPSO satellite)**

457

458 The Cloud-Aerosol Lidar with Orthogonal Polarization (CALIOP) is a two-wavelength polarization lidar  
459 (1064 and 532nm) ~~aboard the Cloud-Aerosol Lidar and Infrared Pathfinder Satellite Observations~~  
460 ~~(CALIPSO)~~ that performs global profiling of aerosols and clouds in the troposphere and lower  
461 stratosphere. ~~CALIOP is the primary instrument on the Cloud-Aerosol Lidar and Infrared Pathfinder~~  
462 ~~Satellite Observations (CALIPSO) satellite. CALIOP is required to accurately measure~~ measures signal  
463 returns in a large range, from ~~the~~ aerosol-free region ~~between 30 and 35 km as well as the strongest~~ up to  
464 strong cloud returns. ~~Samples acquired~~ The CALIOP profiles are given below 40 km for the 532-nm  
465 channel and below 30 km for the 1064-nm channel ~~are downlinked as profile data.~~ Data used  
466 here acquisition in this research was based on level 2 version 4-10 CALIPSO product, of 532 nm  
467 wavelength with a spatial resolution of 5 km (20N-50N, 20E-50E) and vertical resolution of 60 m (limited  
468 up to 6 km).

469

470

471

472

473

474

475

476

477

478

479

480

481



### 3. Results and discussion

The following description of the dust event will proceed chronologically from 7 to 10 September and include main findings ~~offrom~~ the different measuring instruments (Sect. 2). The order of the instruments described follow the most interesting features revealed, not necessarily in the same order for each day. We provide 2D ceilometer plots (height vs. time) presenting the extreme dust plume decent only from ~ 1km ASL due to the ceilometer limitation to detect signals from higher levels (explained in Sect. 2.1). Unlike the high resolution ceilometers, CALIPSO overpass above Israel was available only on 10 September 2015 revealing dust distribution in various levels up to 5 km ASL.

#### 3.1 7 September 2015

On 7 September, images from MODIS Aqua (Fig. 4a) and MODIS Terra (Fig. 4e) taken between 07:20-12:10 UTC show that the dust plume progressed from northeast in a near-circular motion over the Mediterranean Sea. The penetration of the dust plume to Israel was indicated by AERONET Sede Boker site at ~ 05 UTC by an increase in AOD along a decrease in the Angström exponent (Fig. ~~5) from AERONET Sede Boker site.5)~~. The relationshipconnection between ~~the~~decreasing Angström exponent ~~decreasevalues~~ and the mineral-dust plume was pointed out by Mamouri et al., (2016). ~~They studied the dust layer particule linear depolarization by an EARLINET lidar stationed in Limassol Cyprus and concluded that the-) which presented values of~~ linear depolarization ratio ~~of~~between 0.25-0.32 on 7, and 10 September, ~~indicated~~indicating the dominance of ~~the~~-mineral dust. In addition, an increase in the PM concentration started at ~ 05 UTC (not shown) reaching the highest hourly values of  $107 \mu\text{g m}^{-3}$  PM<sub>2.5</sub> (Table 5) and  $491 \mu\text{g m}^{-3}$  PM<sub>10</sub> (Table 6) only in the Jerusalem elevated sites (~ 800 m ASL) and only at 22 UTC. This 17-hour gap is shown by the ceilometers' plots (Fig. 6-12) ~~of~~as a downward motion of the dust plume from ~ 04 UTC in all measuring sites except for the elevated Mount Meron site (1150 m ASL, Fig. 13). Following Gasch et al (2017) cold pool outflows concept, the exception of Mount Meron site is supported by the MSG-SEVIRI picture (Fig. 14) showing that the first dust plume was fragmented (Fig.14, red arrow) and the second dust plume (Fig.14, black arrow) had not passed over Israel before 12 UTC. The deep blue scale evident in all Mount Meron ceilometer plots (Fig. 13) indicate total attenuation distinctively from 7 September ~ 14 UTC to 8 September ~ 16 UTC. However, due to the complexity of the dust plume progress (further shown) and the weak signal counts shown up to 3.5 km ASL (before 7 September ~ 14 UTC and after 8 September ~ 16 UTC), the assumption of a total attenuation throughout



515 the period analysed is uncertain. Unfortunately, we did not have auxiliary measurements from the Mount  
516 Meron region to justify our assumptions.

517

518 ~~The full picture of what happened on the 7 September can be further obtained from~~ While the  
519 MSG-SEVIRI picture at 12 UTC ~~that~~ shows AOD values to be ~~still~~ under 1 in most parts of Israel (Fig.  
520 ~~15~~), the PM concentrations on ground level were found to be bearable (up to 105  $\mu\text{g m}^{-3}$  PM<sub>2.5</sub> and  
521 305  $\mu\text{g m}^{-3}$  PM<sub>10</sub>, mainly in the Jerusalem elevated sites). At ~~the same time~~ 12 UTC, Beit Dagan  
522 radiosonde profiles show ~~the a characteristic MLH was still high (of 700 m ASL,~~ (Fig. 16).  
523 ~~And,~~ Moreover, at 23 UTC the formation of clouds was indicated by ceilometers' profiles ~~at 23 UTC~~ (Fig.  
524 17 a) ~~show indications of typical cloud presence from~~ at 400 m ASL in the shoreline ~~site~~ (Tel Aviv, 5 m  
525 ASL) and up to ~700 m ASL in the elevated southern site (Nevatim, 400 m ASL). Clouds are identified  
526 by the peak shape of the ceilometer profiles (Uzan et al, 2016) and the high ~~attenuated backscatter~~ range  
527 corrected signal of  $10^{-1} \text{ m}^{-1} \text{ sr}^{-1}$  which in this case ~~is~~ was 4 orders of magnitude higher than the ~~attenuated~~  
528 ~~backscatter~~ range corrected signal of the dust plume (shown in Fig 17 b-c). ~~In spite of the still high MLH~~  
529 ~~and the cloud presence, the~~ Hourly solar radiation measurements ~~clearly indicates the significance~~ (Fig.  
530 18, see 7 September daily plot) from Beit Dagan (central site) and Beer Sheva (southern site) show a  
531 significant effect of the dust plume ~~effect through the~~ by a decrease ~~of the daily~~ in direct radiation along  
532 with an increase of ~~the~~ diffuse radiation ~~(Fig. 18, see 7 September daily variation) measured both in~~  
533 ~~central Israel (Beit Dagan) and southern Israel (Beer Sheva).~~

534

535

536

537

538

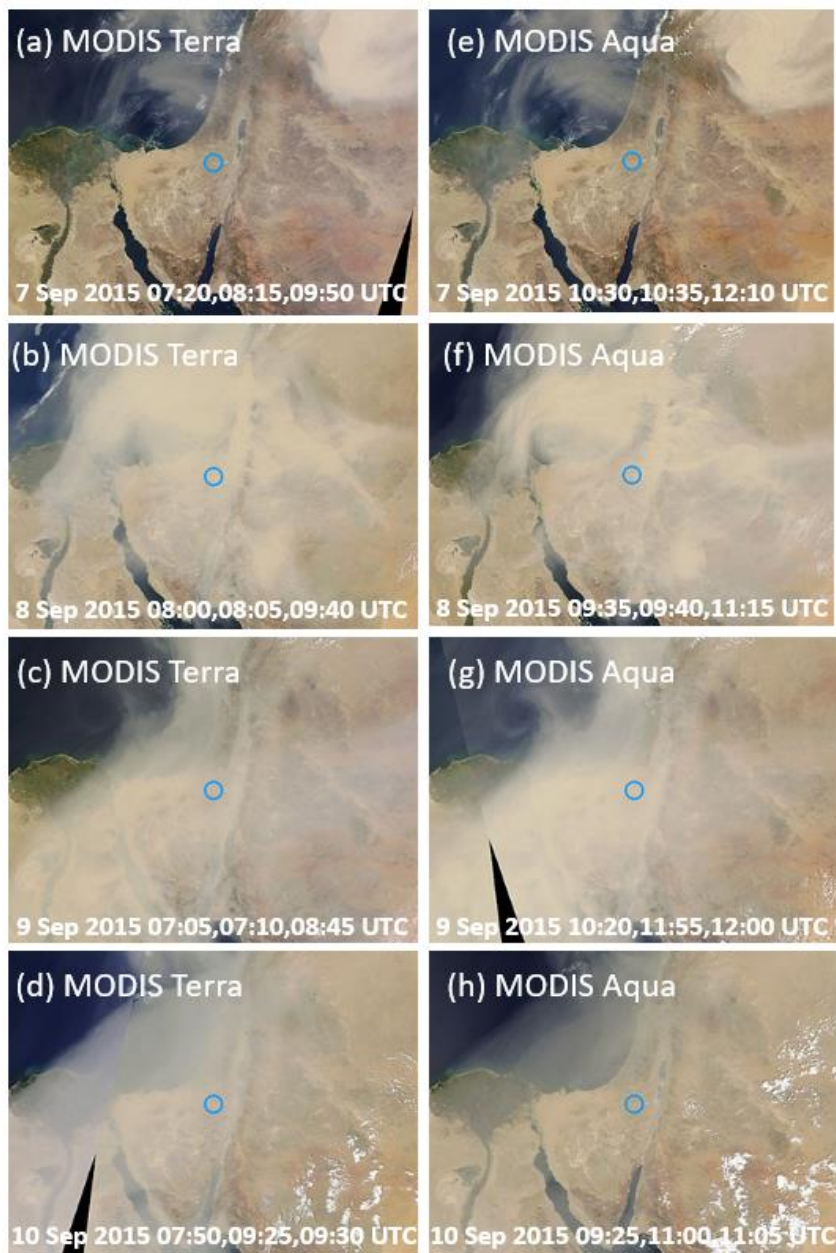
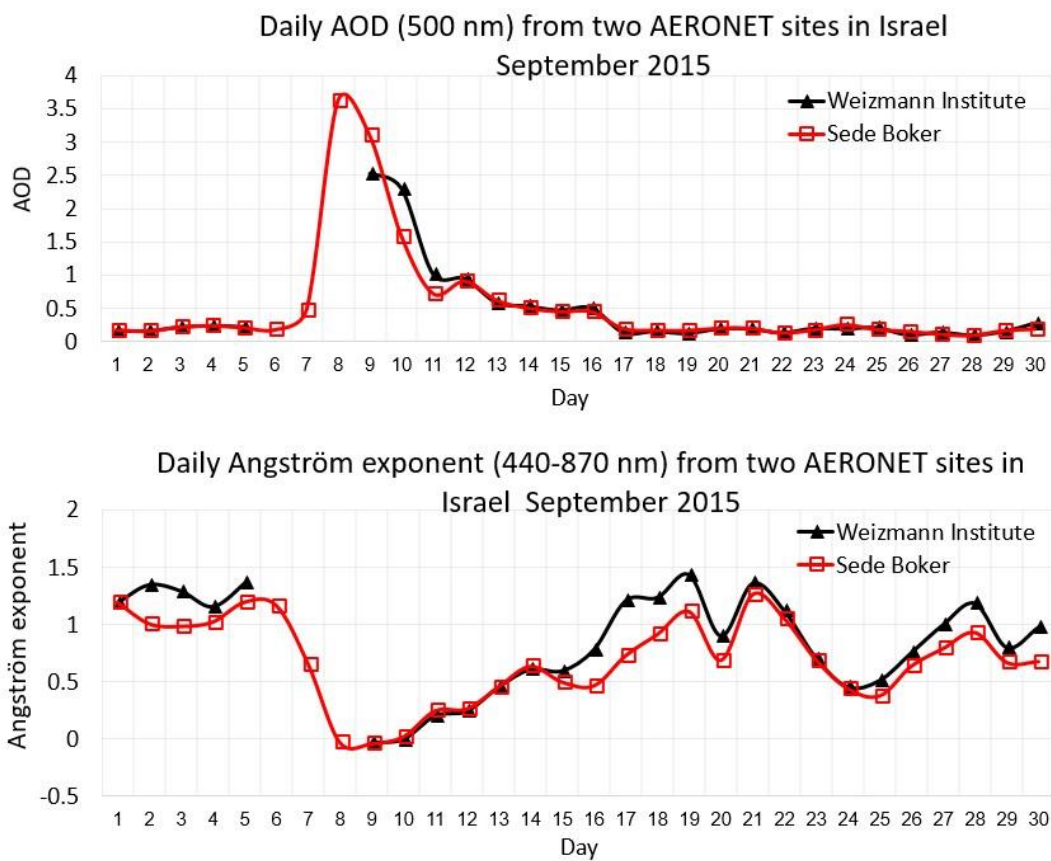


Figure 4. Pictures from MODIS terra (a-d) and MODIS Aqua (e-h). The date and time of overpass are indicated on each figure. The blue circle indicating the location of the AERONET Sede Boker site. Source: <https://aeronet.gsfc.nasa.gov>.

539  
540  
541  
542  
543  
544  
545  
546  
547  
548  
549  
550

551

552



553

554

555

556

557

558

559

560

561

562

563

564

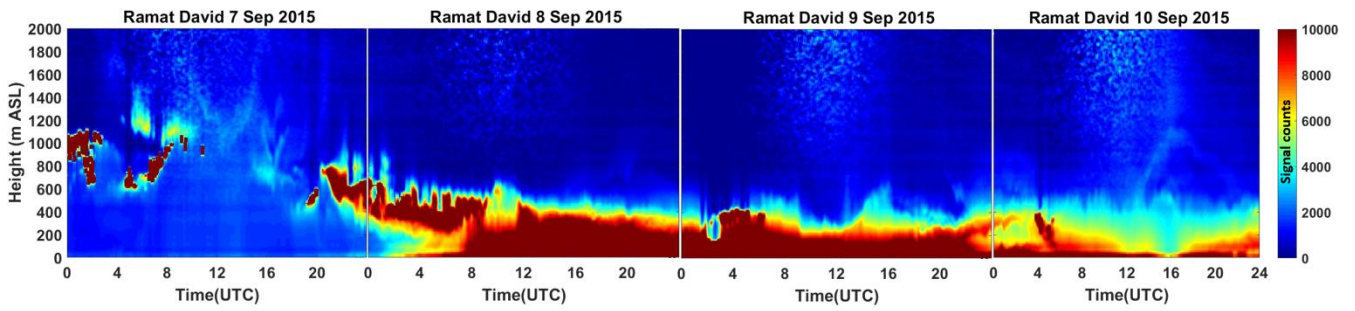
565

566

567

568

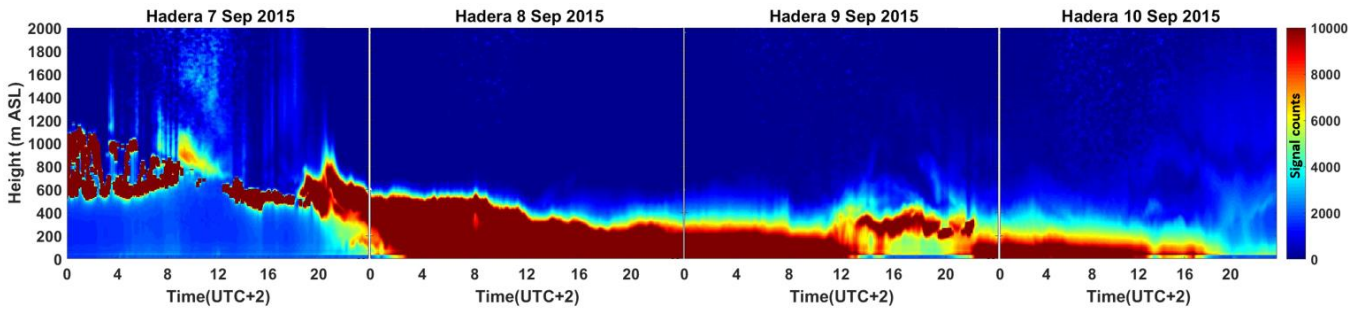
Figure 5. September 2015 daily average of AOD (top panel) and Angström exponent (bottom panel) from two AERONET sites in Israel (Sede Boker and Weizmann, see Fig.3). The Weizmann AERONET did not operate on 6-8 September due to power failure.



569

570 Figure 6. Ramat David ceilometer signal counts plots for 7-910 September 2015. Y-axis is the height  
 571 up to 2000 m ASL, X-axis is the time in UTC, signal count scale range between 0-10,000.

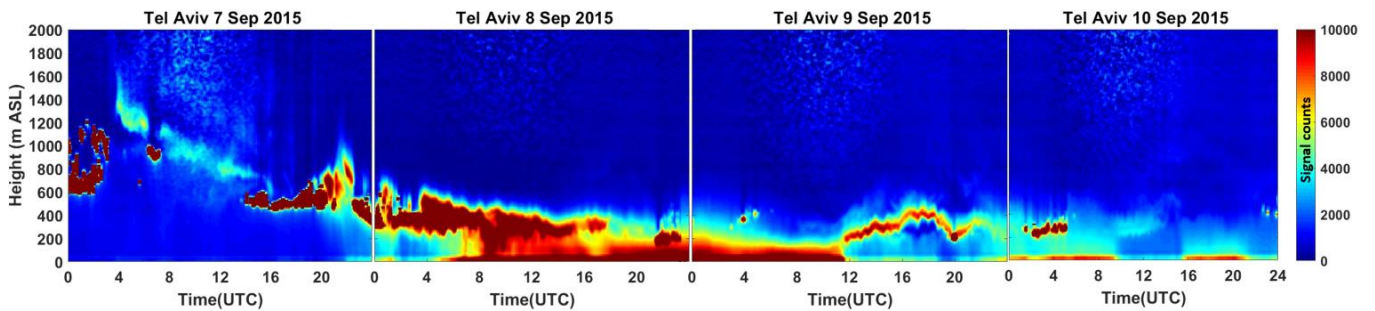
572



573

574 Figure 7. Hadera ceilometer signal counts plots for 7-910 September 2015. Y-axis is the height from  
 575 site deployment to 2000 m ASL, X-axis is the time in LST (UTC+2), signal count scale range between  
 576 0-10,000.

577



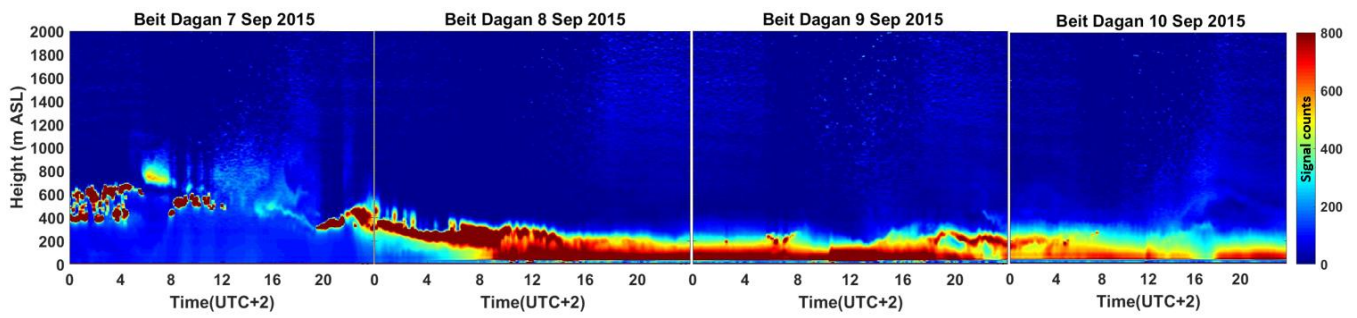
578

579 Figure 8. Tel Aviv ceilometer signal counts plots for 7-910 September 2015. Y-axis is the height from  
 580 site deployment to 2000 m ASL, X-axis is the time in UTC, signal count scale range between 0-  
 581 10,000.

582

583





584

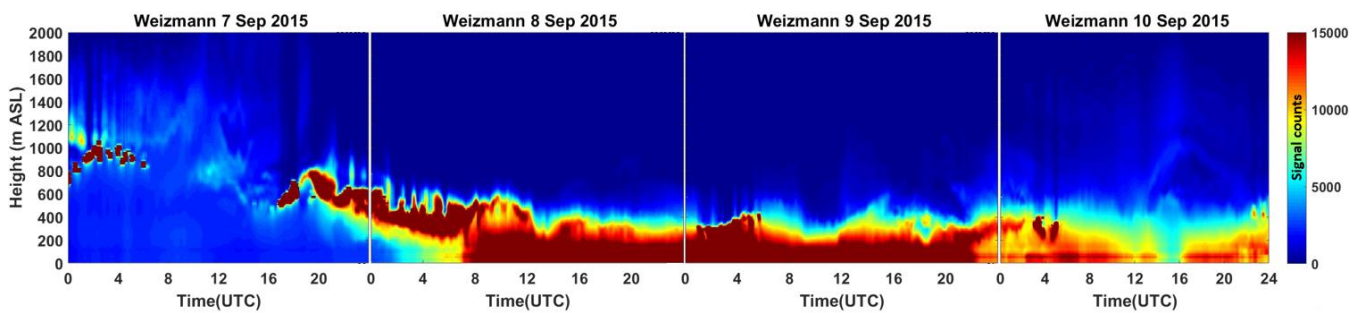
585

586

587

588

Figure 9. Beit Dagan ceilometer signal counts plots for 7-9<sup>10</sup> September 2015. Y-axis is the height from site deployment to 2000 m ASL, X-axis is in LST (UTC+2), signal count scale range between 0-800.



589

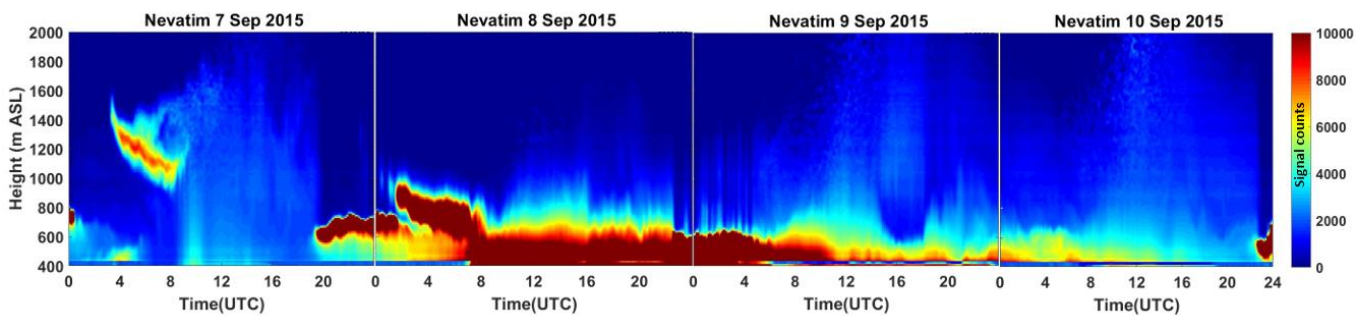
590

591

592

593

Figure 10. Weizmann ceilometer signal counts plots for 7-9<sup>10</sup> September 2015. Y-axis is the height from site deployment to 2000 m ASL, X-axis is in UTC, signal count scale range between 0-15,000.



594

595

596

597

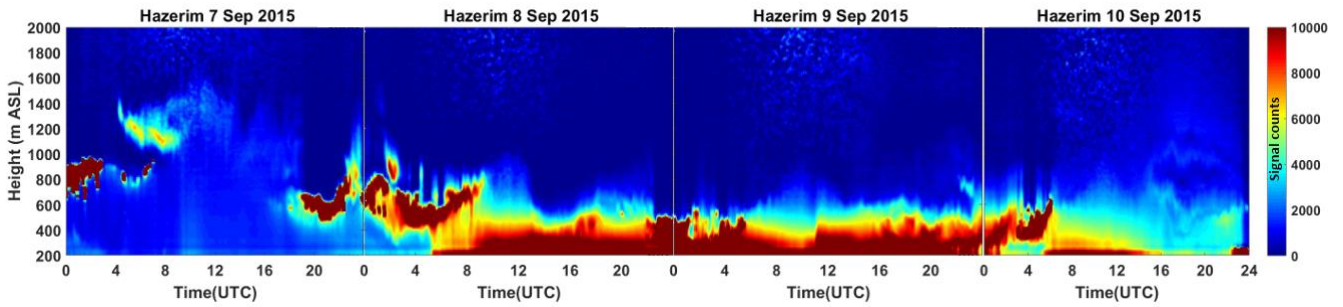
598

599

600

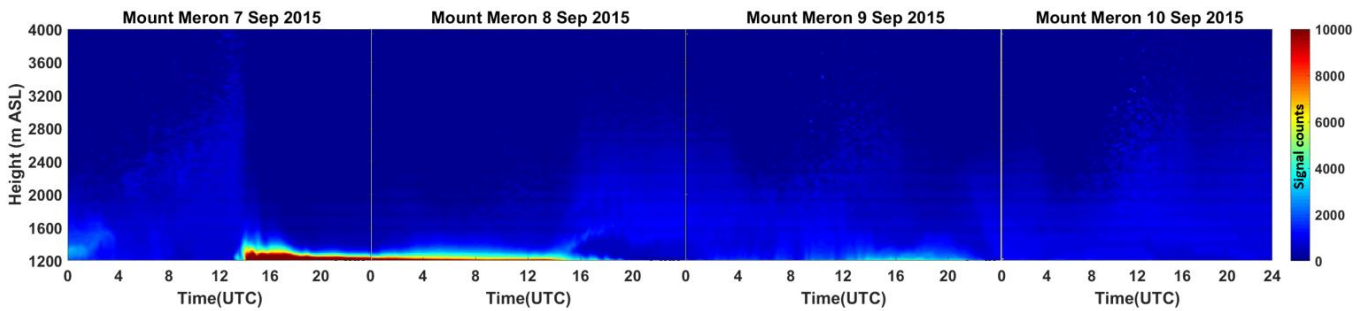
601

Figure 11. Nevatim ceilometer signal counts plots for 7-9<sup>10</sup> September 2015. Y-axis is the height from site deployment to 2000 m ASL, X-axis is the time in UTC, signal count scale range between 0-10,000.



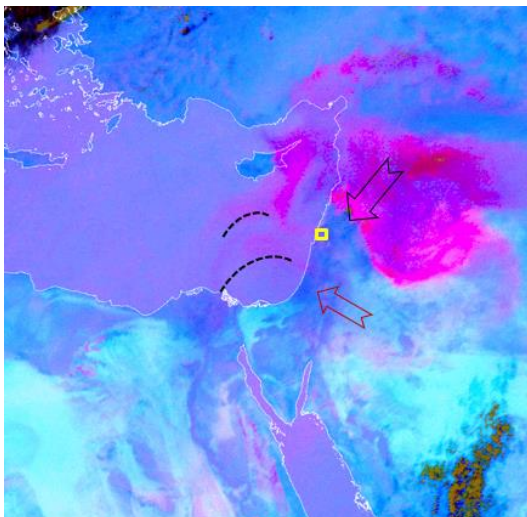
602  
603  
604  
605  
606  
607

Figure 12. Hazerim ceilometer signal counts plots for 7-~~9~~10 September 2015. Y-axis is the height from site deployment to 2000 m ASL, X-axis is the time in UTC, signal count scale range between 0-10,000.



608  
609  
610  
611  
612  
613  
614

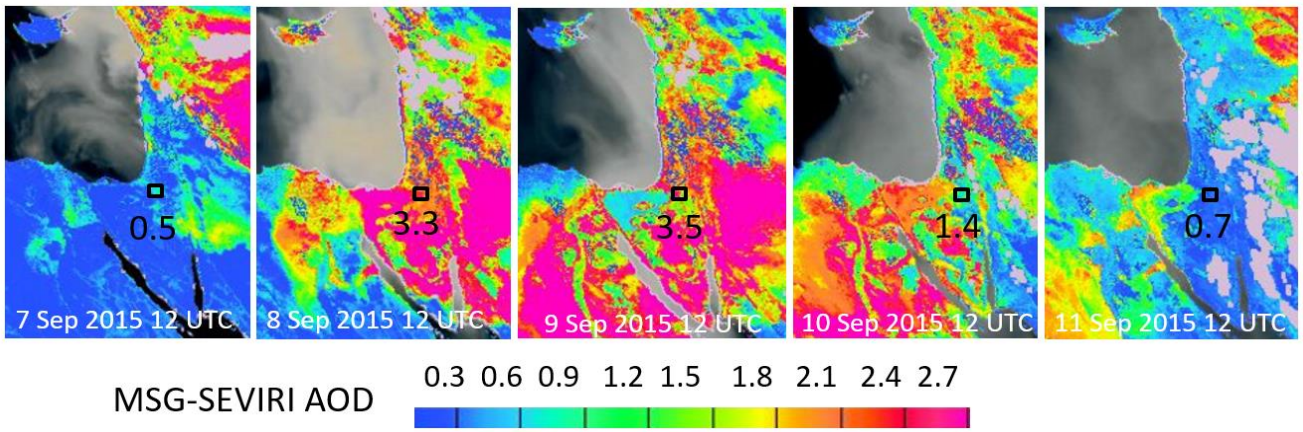
Figure 13. Mount Meron ceilometer signal counts plots for 7-~~9~~10 September 2015. Y-axis is the height from site deployment to ~~2000~~4000 m ASL, X-axis is the time in UTC, signal count scale range between 0-10,000.



615  
616  
617  
618  
619

Figure 14. Picture from MSG-SEVIRI satellite of the dust RGB component (dust appears in pink colors) at ~~12 UTC~~on 7 September 2015 12 UTC with indications of Mount Meron ceilometer site (yellow square, Lon 33.0°, Lat 35.4°) and the dust plumes progression from east to west (red arrow and dashed lines) and from the northeast to southwest (black arrow).





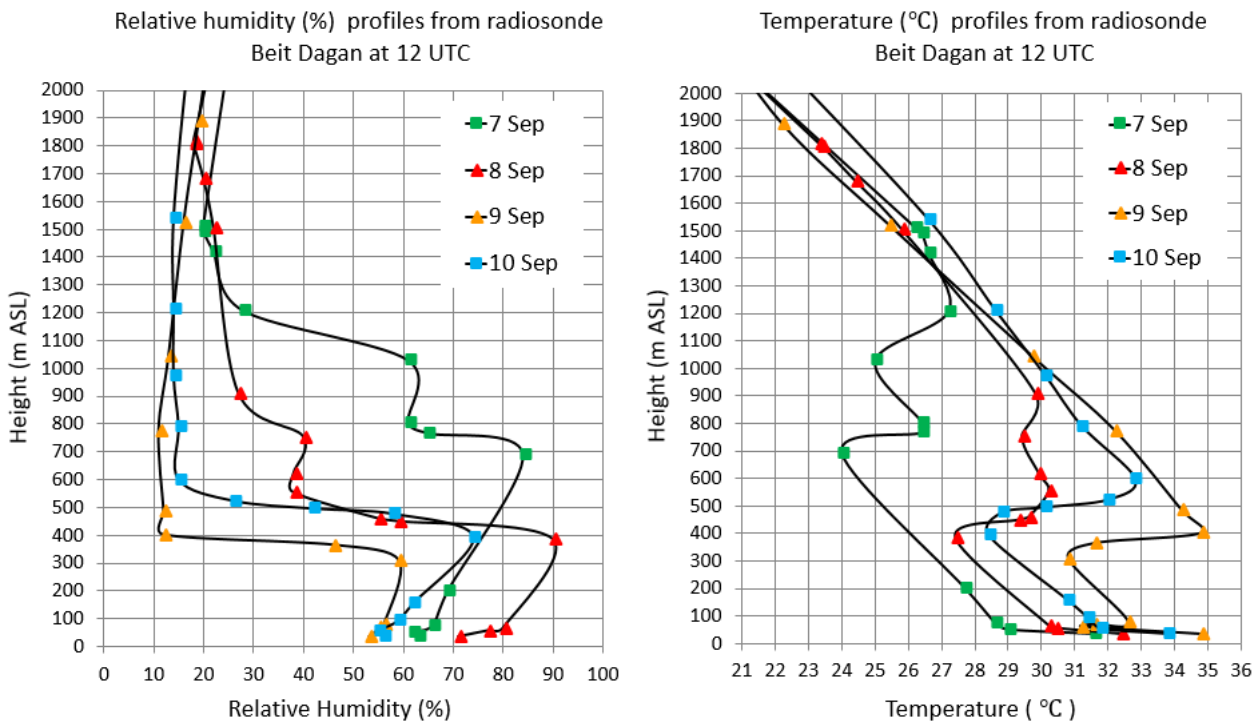
620

621

622 Figure 15. Aerosol Optical Depth (AOD) at 12 UTC 7-11 September 2015 analyzed by  
 623 [NAScubeNASCube](#) (Université de Lille) based on imagery from the MSG-SEVIRI satellite (by a  
 624 combination of the SEVIRI [channels](#) IR8.7, IR10.8 and IR12.0-[channels](#)). The map includes indication  
 625 of the Sede Boker AERONET site (black square) and its AOD value at 12 UTC.

626

627

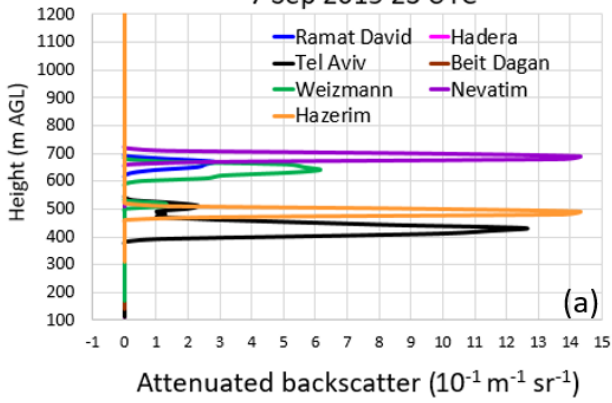


628

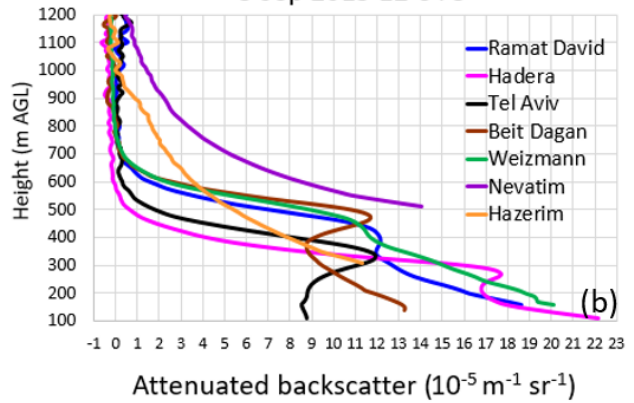
629 Figure 16. Radiosonde Beit Dagan profiles at 12 UTC between 7-10 September 2015 of relative  
 630 humidity (left panel) and temperature (right panel).

631

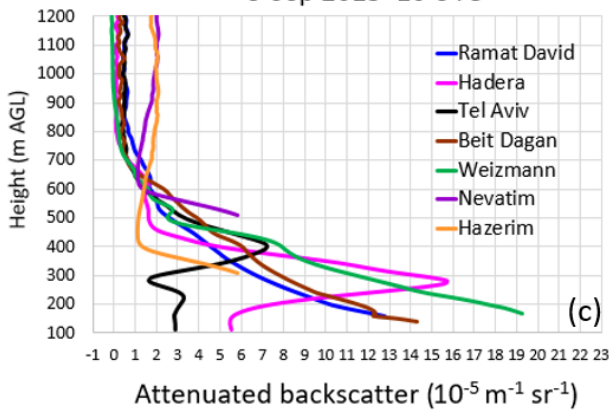
Ceilometer profiles from 7 sites  
7 Sep 2015 23 UTC



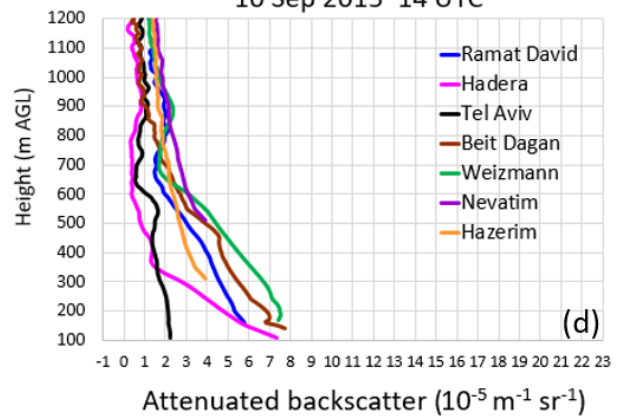
Ceilometer profiles from 7 sites  
8 Sep 2015 12 UTC



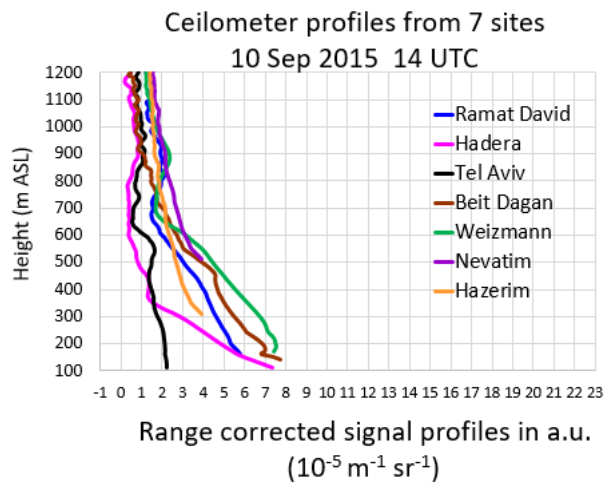
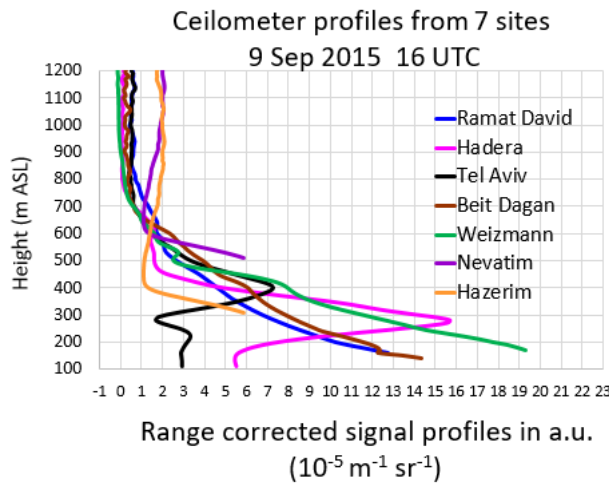
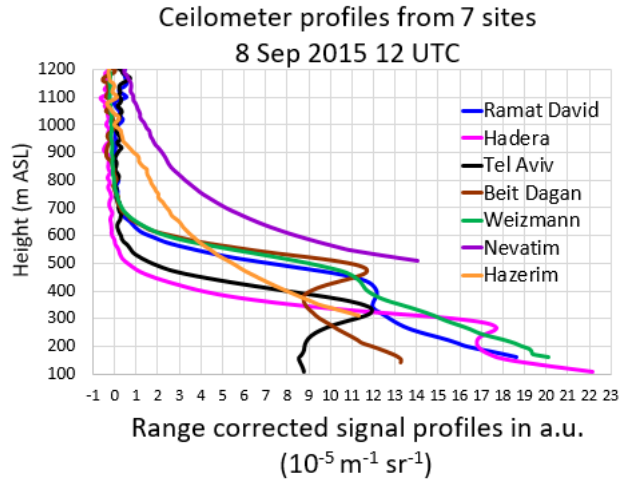
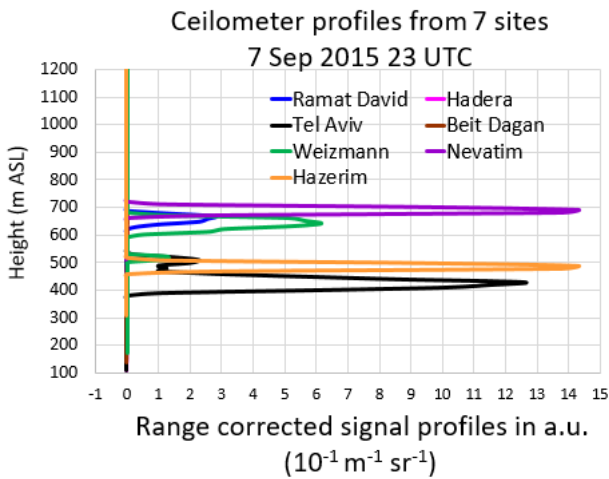
Ceilometer profiles from 7 sites  
9 Sep 2015 16 UTC



Ceilometer profiles from 7 sites  
10 Sep 2015 14 UTC



632



633

634

635

636

637

638

639

640

641

642

643

644

Figure 17. Ceilometer ~~attenuated backscatter~~ range corrected signal profiles (in arbitrary units) from 7 sites (Ramat David, Hadera, Tel Aviv, Beit Dagan, Weizmann, Nevatim and Hazerim, [see locations in Fig. 3](#)) at ~~23 UTC~~ on 7 Sep 2015 23 UTC (a), 8 September 2015 ~~at~~ 12 UTC (b), 9 September 2015 ~~at~~ 16 UTC (c) and 10 September 2015 ~~at~~ 14 UTC (d). Notice each profile begins ~~relative~~ relativily to the height of its' measuring site (ASL) including a deletion of data from the first 100 m AGL due to inaccuracies in the first range gates of the ~~CL31~~ ceilometers (for details see Sect. 2.1). Fig (a) shows cloud detection therefore it hasis given in a different scale ( $10^{-1} \text{ m}^{-1} \text{ sr}^{-1}$ ) and a different x-axis range.

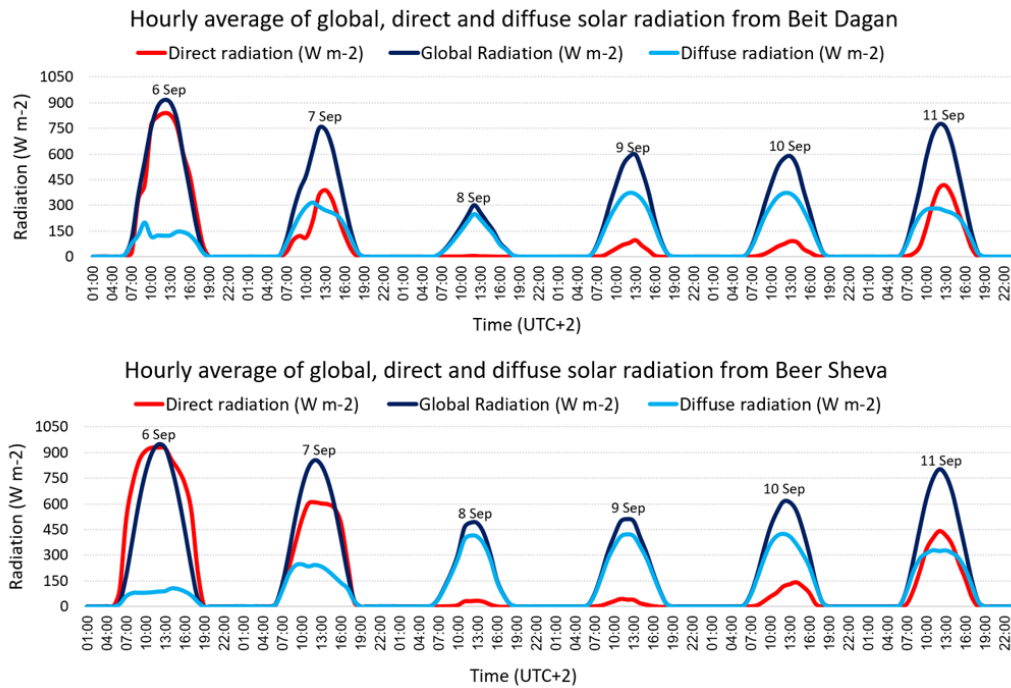


Figure 18. Hourly average of global, direct and diffuse solar radiation between 6-11 September 2015 from Beit Dagan and Beer Sheva.

### 3.2 8 September 2015

The main phase (the peak) of the dust storm occurred on 8 September. Images from MODIS Aqua (Fig. 4b) and MODIS Terra (Fig. 4f) taken between 08:00-11:15 UTC show the dust storm prevaleenceprevailed over Israel. Ceilometers' plots detect the descending motion of the dust plume reached ground level at ~ 08 UTC (Fig. 6-12). Simultaneously, Sede Boker AERONET AOD measurements increased up to ~4 along with a negative Angström exponent (not shown).

An hour later, at ~ 09 UTC, extreme maximum PM hourly values were measured in the elevated sites of Jerusalem Safra ( $10,280 \mu\text{g m}^{-3}$  PM10) and Jerusalem Bar Ilan ( $3,063 \mu\text{g m}^{-3}$  PM2.5). Whereby, in the coast and the lower northern regions, maximum PM values were measured only 14 hours later at ~23 UTC and were much lower (up to  $3,459 \mu\text{g m}^{-3}$  PM10 and  $470 \mu\text{g m}^{-3}$  PM2.5, see Tables 5-6). Fig. 19 illustrates the spatio-temporal variation of the PM10 extreme values, beginning at ~ 12 UTC in the elevated Jerusalem sites and ending at midnight in the shoreline.

Ceilometer At ~08 UTC ceilometer plots from Tel Aviv, Beit Dagan, Weizmann and Hadera (with plots higher scale range of 0-15,000, not shown here), Beit Dagan and Weizmann,) reveal a two-an

667 ~~ununiformed dust layer shape~~, (beneath and above ~ 300 m ASL) ~~starting from ~08 UTC. This two-layer~~  
668 ~~shape later on that eventually~~ combined into one dense layer. This ~~pattern process~~ may explain the spatial  
669 variation and time delay between the extreme PM measurements in the elevated vs. lower sites.

670 ~~Referring to satellite imagery on 8 September,~~

671 MSG-SEVIRI at 12 UTC (~~Fig. 15~~) ~~underestimated~~estimated AOD to be 2.7 while Sede Boker  
672 AERONET measured a higher value of 3.3- (~~Fig. 15~~). Furthermore, MODIS images (Fig. 4a, 4b) show a  
673 dominant dust plume over Israel, ~~while whereas~~ solar global radiation measurements (Fig.20a)  
674 ~~show present~~ significant spatial variations ~~in the reduction of the global radiation measured in the different~~  
675 ~~regions. Minimum as minimum~~ values (down to 200 W m<sup>-2</sup>) were measured mainly in northern Israel.  
676 ~~This may infer the complex behavior of the dust dispersion in contrary to satellite imagery of a prevailing~~  
677 ~~dust storm over Israel.~~ Additionally, in spite the extreme PM10 values of 9,031 µg m<sup>-3</sup> measured in the  
678 elevated southern site (Negev Mizrahi 577 m ASL, Table 6), the maximum global radiation in southern  
679 Israel was still relatively high (~500 W m<sup>-2</sup>). Generally, the radiative transfer analysis during heavy dust  
680 loads is complicated and relies on several parameters such as size, structure and composition of the  
681 aerosols (Bauer et al, 2011). Dense dust layers such as in this extreme dust storm definitely had an impact  
682 on the radiation budget hence changing weather patterns and air mass transport. The spatial variation of  
683 ground level measurements compared to the quit uniform picture revealed by the satellites may infer the  
684 complexity of the dust plume evolution.

685  
686 Overall, 8 September shows the highest PM concentrations and the lowest solar radiation levels  
687 for this dust storm event. The solar radiation was composed mainly of diffuse radiation (Fig.18)  
688 emphasizing the immense atmospheric dust loads preventing direct insolation. Surprisingly, the low solar  
689 radiation was still ~~able capable~~ to warm the ground and generate a late and weak sea breeze front (not  
690 shown). We assume the insufficient ground heating generated weak thermals that ~~were too weak to create~~  
691 ~~and could not~~ inflate a MLH. Therefore, we assume the low MLH (300 m ASL) revealed by ~~the radiosonde~~  
692 Beit Dagan profiles from 8 September (Fig.16) ~~which~~ may indicate the dust plume base height. As a  
693 result, the ceilometers' plots were fully attenuated above ~300 m ASL.

694  
695  
696  
697



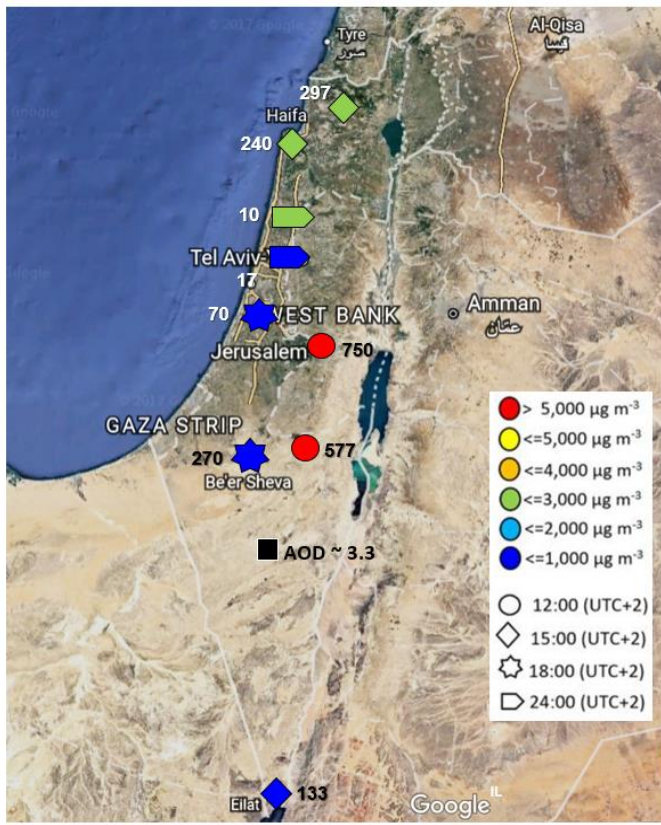
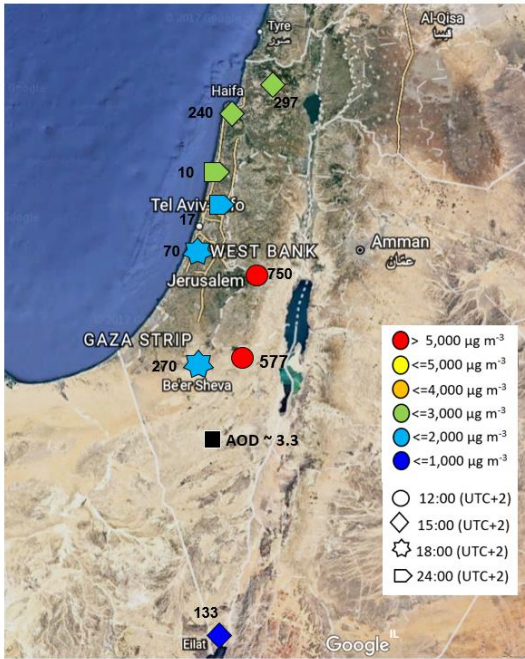
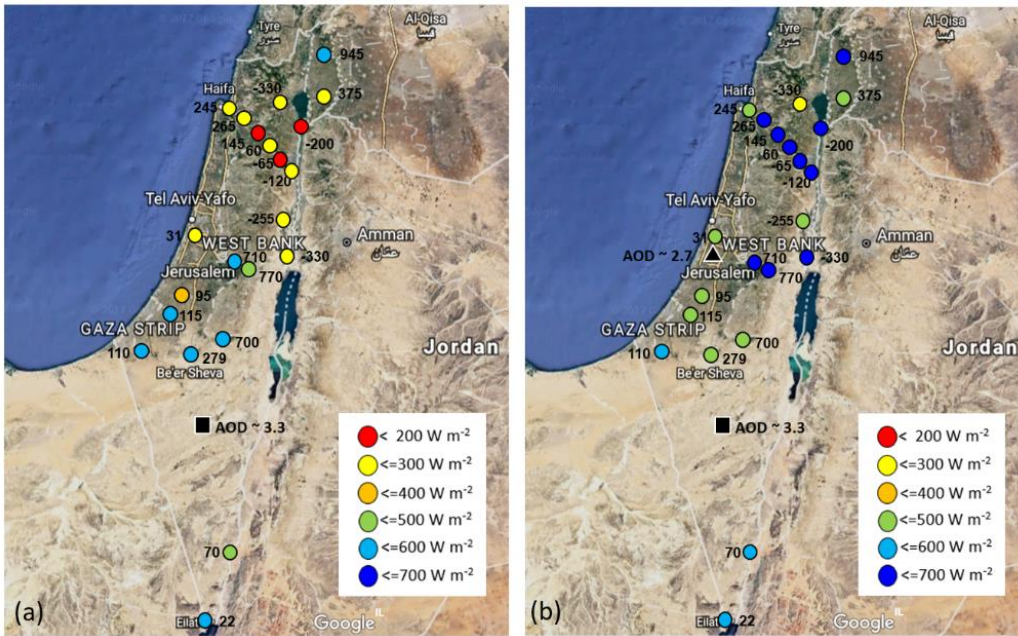
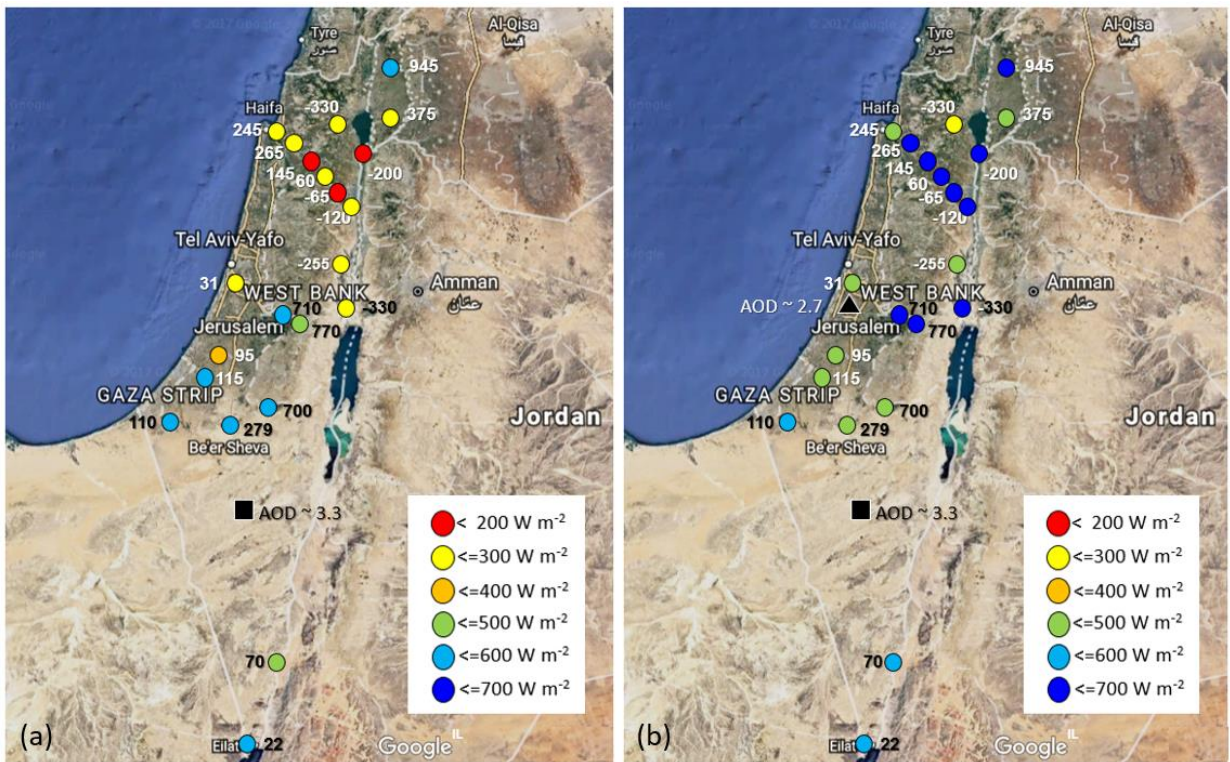


Figure 19. A map of PM10 maximum hourly ~~concentration~~ concentrations from 9 sites measured at 10 UTC on 8 September 2015, 10 UTC (midday). The map includes indications of the time of measurement (symbol shape), concentration range (symbol color), height of measurement site (numbers in black on map) and AERONET AOD from AERONET Sede Boker site.





705



706

707

708

709

710

711

712

713

714

Figure 20. A map of maximum global solar radiation from 22 sites measured at 10 UTC (midday) on 8 September 2015 (a) and on 9 September 2015 (b). The map includes indications of radiation range (see legend), height of measurement site (numbers in black on the map) and AERONET AOD from AERONET Sede Boker site (black square) and Weizmann site (black triangle). On 8 September the AERONET in Weizmann AERONET site did not operate due to power failure.

### 3.3 9 September 2015

On 9 September, MODIS images (Fig.4c and 4g) taken between 07:05-12:00 UTC show the dust plume progression southward to Egypt (Fig. 4), indicated by Sede Boker AERONET AOD  $>3$  and along a negative Angström exponent (Fig. 5). ~~Again, an underestimation of At 12 UTC AOD from MSG-SEVIRI at 12 UTC shows lower AOD is~~  $\sim 2.7$  ~~compared to~~ whereas Sede Boker AERONET AOD reached up to  $\sim 3.5$  (Fig.15). In contrary to the high AOD measurements, and the descend of the MLH down to  $\sim 350$  m ASL (Fig.16), PM values did not ~~crease~~ increase but rather decrease below  $900 \mu\text{g m}^{-3}$  PM<sub>2.5</sub> (Table 5) and  $4050 \mu\text{g m}^{-3}$  PM<sub>10</sub> (Table 6). The drop in PM concentration gave rise to an increase of solar radiation ~~of~~ up to  $400 \text{ W m}^{-2}$  (Fig. 20 b). An increase in solar radiation enables significant ground heating to ~~temperature~~ values measured prior to the initiation of the dust storm (not shown). Thus, allowing generation of thermals and the creation of a late the sea breeze cycle ~~which~~ (Uzan et al., 2016). The entrance of the sea breeze front between 11- 12 UTC eventually produced ~~an arc shape~~ a narrow dust layer ascent visible in mainly in the coastline -Tel Aviv and Hadera ~~coastal~~ ceilometers ~~beginning at~~ 12 UTC (Fig.7-8). Interestingly, on 9 September, compared to the peak of the dust storm on the day before, we do not see a significant difference in solar radiation in southern Israel, which continued to be relatively high  $\sim 500 \text{ W m}^{-2}$  (Fig. 20b).

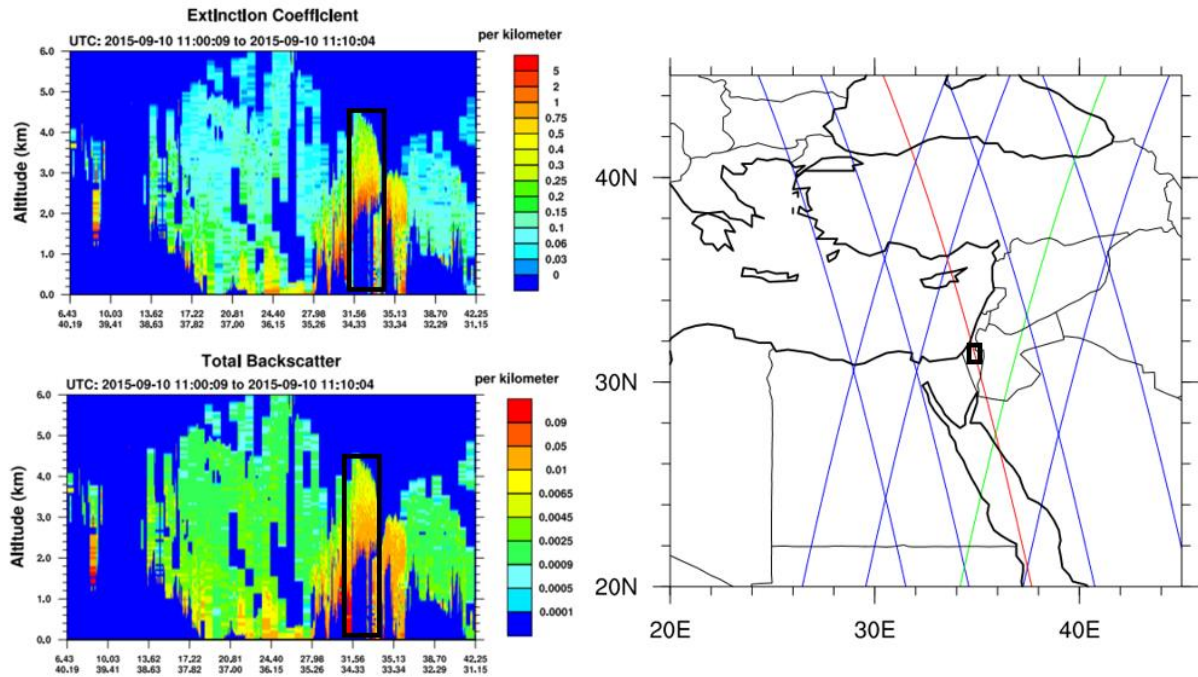
### 3.4 10 September 2015

On 10 September, MODIS pictures from 7:50 -11:05 UTC (Fig. 4d and 4h) show the dust plume over Israel transported southeast from Syria-Iraq to Sinai-Egypt. The CALIPSO single overpass Israel at 11:00-11:10 UTC revealed a dust layer ~~between 2-4~~ up to 5 km ASL (Fig.21). This corresponds with the EARLINET lidar measurements in Limassol, Cyprus (Mamouri et al., 2016) detecting a dust plume between 1-3 km ASL. We assume the CALIOP lidar did not produce data beneath 2 km ASL due to total attenuation. Fortunately, the ceilometers complement the dust profile (beneath ~~1~~  $\sim 1$  km ASL) showing a reduction both in signal counts (Fig. 6-12) and in ~~attenuated backscatter~~ range corrected signal profiles (Fig.17d) pointing out a reduction in atmospheric dust loads. AOD from MSG-SEVIRI and Sede Boker AEONET show a decrease down to ( ~~$\sim 1.5$~~ ) and a low Angström exponent of  $\sim 0.5$  indicating prevalence of mineral dust.

~~Furthermore, a~~ A profound reduction in PM values, down to a third of the values from the day before (Table 6), was measured evident mainly in southern Israel. Therefore, an increase in direct radiation (~~therefore an increase in global radiation as well~~) was measured in southern site ~~as well~~ (Fig.18).

749 The reduction of dust loads may also be denoted by the orange background color of the photograph taken  
 750 ~~on the~~ 8 September (Fig.1b) compared to the grey background visible on 10 September (Fig.1c). As the  
 751 dust storm dissipated, cloud formation (indicated by brown spots and evaluated by ceilometer profiles -  
 752 not shown) was visible from ~~at~~ ~4 UTC by ceilometers ~~plots from~~ Ramat David (Fig.6), Tel Aviv (Fig.8),  
 753 Weizmann (Fig.10) and Hazerim (Fig.11) ~~(indicated by brown spots and evaluated by ceilometer profiles~~  
 754 ~~-not shown), otherwise).~~ the clouds formation was not evident by MODIS imagery (Fig 4d, 4h).

755  
 756  
 757  
 758  
 759  
 760



761



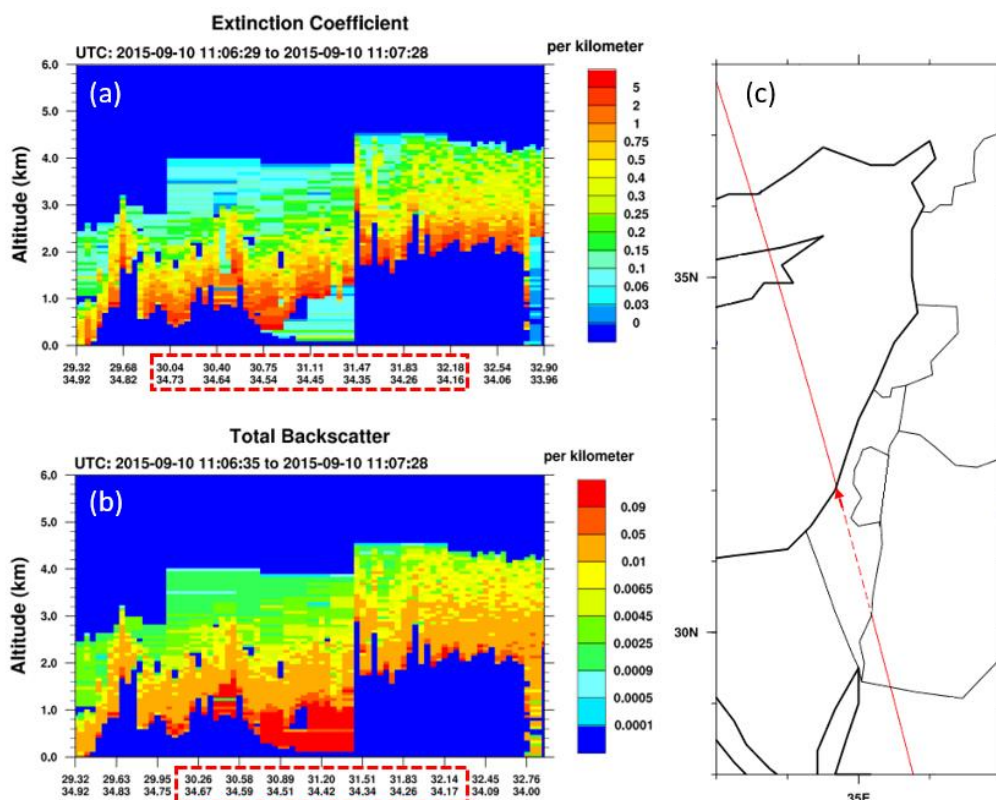


Figure 21. (c) A map of the EM centered on Israel with indication of CALIPSO satellite overpasses (right panel). The only overpass above Israel was from south-east to north-west (red line) on 10 September 2015 at 11:00-11:10 UTC (indicated by a red line). On the left panel are the CALIOP lidar products of total backscatter and (from 532 nm wavelength) of extinction coefficient. Indications of the overpass (a) and total backscatter (b) are given along the path over Israel is given by a black rectangle (dashed red line). The ground elevation begins from -20 m ASL in the southeastern point. A quarter of the way through ground level rises up to ~ 600 m ASL and then gradually declines to sea level height as it reached shoreline in the northwestern point.

As in the attempt to determine the "end" of the dust storm continues to dissipate over Israel, we analyzed measurements from all instruments regarding (Sect. 2) seeking values that were measured prior to the dust storm penetration. While AERONET AOD values (Fig.5), solar radiation measurements (not shown) and satellite imagery from MODIS and SEVIRI (not shown) detect indicate clearance of the dust storm on 17 September. PM On the other hand, PM values and ceilometer profiles indicate indicated the dust storm ended 4 days earlier at on 13 September (not shown). This The difference between the measurements that include atmospheric layers aloft (satellite imagery, solar radiation and AOD AERONET) compared to measurements limited to the lower atmosphere (PM values and ceilometers)

782 postulates a scheme of ~~two~~several dust ~~levels~~layers or multiple sources of the dust plumes, which may  
783 support similar conclusions from previous studies (Stavros et al, 2016; Mamouri et al, 2016, Gasch et al,  
784 2017).

## 793 4. Conclusions

794  
795 A very severe dust storm struck the EM on September 2015. Previous investigations  
796 ~~including presented~~ in-situ and remote sensing measurements ~~and models~~, discussed the initiation of the  
797 dust storm in the Syrian-Iraqi border, aspects of its transport over the EM and the limitations of the  
798 models to forecast this unique event, ~~and several aspects of its transport over the EM.~~ The analysis  
799 concentrated mainly on the upper level of the atmosphere ~~and analyzed at~~ specific time segments of the  
800 dust storm ~~period~~. The benefit ~~here of this study~~ is the provision of continuous measurements of vertical  
801 dust profiles of the dust in the lower part of the troposphere ~~and from 8 ceilometer sites. The data presented~~  
802 here can be used as a tool to verify state of the art model simulations and provide a different point of  
803 view to the continuous measurements at 8 sites in Israel meteorological conditions governing the dust  
804 plume advection over the EM.

805  
806 ——— This study confirmed that the dust storm entered Israel on 7 September and showed the  
807 gradual downfall of the dust plume from ~1000m ASL on 7 September down to ~400 m ASL on 8  
808 September. The detailed ceilometer profiles and auxiliary instruments enabled to separate the dust storm  
809 into ~~two separated~~ dust layers (beneath and above 1 km) ~~and show a complex dispersion which would~~  
810 ~~have been challenging for meso-scale model simulations.~~ As the dust plume descended towards ground  
811 level on 8 September, PM concentration increased in the elevated stations (up to 10,280  $\mu\text{g m}^{-3}$  PM10)  
812 and radiation decreased down to ~200  $\text{W m}^{-2}$  mainly in the northern region. ~~On 9 September as the dust~~  
813 ~~plume diluted, in spite of the high AOD >3, the global radiation (mainly comprised of diffuse radiation)~~  
814 ~~increased, thus enabling the ground heating and the creation of a late sea breeze circulation (~12 UTC)~~  
815 ~~visible as dust arcs near the coast sites (Tel Aviv, Hadera and Beit Dagan). On 10 September, the dust~~

816 ~~plume motion continued southwest to Egypt, with indication of a dust layer between 2-4 km measured~~  
817 ~~by CALIPSO overpass. The progress of the dust storm from the Syria-Iraqi border (origin) southwest to~~  
818 ~~Egypt over Israel, continued in two levels. The lower level (up to 1 km ASL) dissipated at 13 September~~  
819 ~~while the level aloft (above 1 km ASL) was observed until 17 September.~~

820

821

822 On 9 September, in spite of the high AOD (above 3), the global radiation (mainly comprised of  
823 diffuse radiation) increased, thus enabling sufficient ground heating for the creation of a late sea breeze  
824 front (between 11-12 UTC). The sea breeze circulation generated a narrow dust layer detached from the  
825 ground in the coastal region (Tel Aviv, Hadera and Beit Dagan).

826

827 On 10 September, the dust plume motion continued southwest to Egypt, indicated by CALIPSO  
828 as dust layers up to 5 km. The end of the dust storm over Israel was indicated on 17 September by satellite  
829 imagery, solar radiation and AOD AERONET, while measurements limited to the lower atmosphere (PM  
830 values and ceilometers) indicated the dust storm ended on 13 September. The difference between the  
831 various instruments suggests a scheme of several dust layers or multiple sources of the dust plumes.

832

833 To conclude, Ceilometers have been found to be a crucial tool in the study of the September dust  
834 storm evolution over Israel. In general, ceilometers provide high resolution data base (temporal and  
835 spatial) that broaden the scope of the atmospheric measurements. Fortunately, as worldwide ceilometer  
836 deployment expands, ceilometers are realized as an essential tool in the analysis of meteorological  
837 phenomena and aerosol transport most valuable in the meso-scale.

838

839

840

841

842

843

844

845

846

847

848

849



## 5. Data availability

PM10 measurements- Israeli Environmental ministry air quality monthly reports:

<http://www.svivaqm.net>.  
~~http://www.svivaqm.net~~

Israeli Environmental ministry air quality monthly reports (in Hebrew):

<http://www.sviva.gov.il/subjectsEnv/SvivaAir/AirQualityData/NationalAirMonitoring/Pages/AirMonitoringReports.aspx>.  
~~http://www.sviva.gov.il/subjectsEnv/SvivaAir/AirQualityData/NationalAirMonitoring/Pages/AirMonitoringReports.aspx~~

Weather reports- Israeli Meteorological Service September monthly report (in Hebrew):

<http://www.ims.gov.il/IMS/CLIMATE/ClimateSummary/2015/hazesept+2015.htm>  
~~http://www.ims.gov.il/IMS/CLIMATE/ClimateSummary/2015/hazesept+2015.htm~~

Radiosonde profiles –University of Wyoming:

<http://weather.uwyo.edu/upperair/sounding.html>.  
~~http://weather.uwyo.edu/upperair/sounding.html~~

AERONET data- <https://aeronet.gsfc.nasa.gov>.

Meteosat Second Generation Spacecraft pictures:

[http://nascube.univ-lille1.fr/cgi-bin/NAS3\\_v2.cgi](http://nascube.univ-lille1.fr/cgi-bin/NAS3_v2.cgi).

<https://www.eumetsat.int/website/home/Images/RealTimeImages/index.html>

Ceilometer profiles- the data is owned by governmental offices. The data is not online and provided by request.

## Author contribution

Leenes Uzan carried out the research and prepared the manuscript under the careful guidance of Smadar Egert and Pinhas Alpert. The authors declare that they have no conflict of interest.

## Acknowledgements

~~We~~For the provision of ceilometer data, we wish to thank the Israeli Meteorological Service (IMS), the Israeli Air Force (IDF), Association of towns for environmental protection (Sharon-Carmel) and Rafat Qubaj from the department of Earth and Planetary Science in the Weizmann institute of Science,~~for their~~  
~~ceilometers' data.~~ Special thanks to Nir Stav (IMS) and Dr. Yoav Levy (IMS) for their fruitful advice, Anat Baharad (IMS) for computer assistance and Pavel Kunin ~~from the~~ (Tel Aviv university) for the CALIPSO images. We thank the principal investigators Prof. Arnon Karnieli and Prof. Yinon Rudich for their effort in establishing and maintaining Sede Boker and Weizmann AERONET sites. We wish to thank the institutes that provide open site data reduction: Université de Lille ~~NASeube-site~~NASCube, Wyoming University Radiosonde ~~site~~ and the Israeli ministry of Environmental protection for the PM data. Partial funding of this research was made by the Virtual Institute DESERVE (Dead Sea Research Venue).

## References

Alpert P., Osetinsky I., Ziv B. and Shafir H.: A new seasons definition based on the classified daily synoptic systems: An example for the Eastern Mediterranean, *Int. J. Climatol.* 24,1013-1021, 2004.

Alpert, P., Ziv, B.: The Sharav cyclone-observations and some theoretical considerations, *Int. J. Geoph. Res.*, 94, 18495-18514, 1998.

Ansmann, A., Petzold, A., Kandler, K., Tegen, I.N.A., Wendisch, M., Mueller, D., Weinzierl, B., Mueller, T. and Heintzenberg, J.: Saharan Mineral Dust Experiments SAMUM-1 and SAMUM-2: what have we learned? *Tellus B*, 63(4), 403-429, 2011.

[Bauer, S., Bierwirth, E., Esselborn, M., Petzold, A., Macke, A., Trautmann, T. and Wendisch, M.: Airborne spectral radiation measurements to derive solar radiative forcing of Saharan dust mixed with biomass burning smoke particles. \*Tellus B\*, 63\(4\), 742-750, 2011.](#)

Bennouna, Y.S., De Leeuw, G., Piazzola, J. and Kusmierczyk-Michulec, J.: Aerosol remote sensing over the ocean using MSG-SEVIRI visible images. *Journal of Geophysical Research: Atmospheres*, 114(D23), 2009.

Continuous measurement of PM10 suspended particulate matter (SPM) in ambient air, Center for Environmental Research Information Office of Research and Development U.S. Environmental Protection Agency Cincinnati, OH 45268 June 1999.

Dayan U., Lifshitz-Golden B., and Pick K.: Spatial and structural variation of the atmospheric boundary layer during summer in Israel-profiler and rawinsonde measurements, *J. Appl. Meteo.* 41, 447-457, 2002.

Derimian, Y., Karnieli, A., Kaufman, Y.J., Andreae, M.O., Andreae, T.W., Dubovik, O., Maenhaut, W., Koren, I. and Holben, B.N.: Dust and pollution aerosols over the Negev desert, Israel: Properties, transport, and radiative effect, *J. Geophys. Res.*, 111, D05205 (1-14), 2006.

Donner, L.J., Wyman, B.L., Hemler, R.S., Horowitz, L.W., Ming, Y., Zhao, M., Golaz, J.C., Ginoux, P., Lin, S.J., Schwarzkopf, M.D. and Austin, J.: The dynamical core, physical parameterizations, and

930 basic simulation characteristics of the atmospheric component AM3 of the GFDL global coupled  
931 model CM3, *Journal of Climate*, 24(13), 3484-3519, 2011.

932  
933 Dubovik, O., A. Smirnov, B. N. Holben, M. D. King, Y. J. Kaufman, T. F. Eck, and Slutsker I.:  
934 Accuracy assessments of aerosol optical properties retrieved from Aerosol Robotic Network  
935 (AERONET) Sun and sky radiance measurements, *J. Geophys. Res.*, 105(D8), 9791–9806, 2000.

936  
937 Gasch, P., Rieger, D., Walter, C., Khain, P., Levi, Y., Knippertz, P., and Vogel, B.: Revealing the  
938 meteorological drivers of the September 2015 severe dust event in the Eastern Mediterranean,  
939 *Atmos. Chem. Phys.*, 17, 13573-13604, 2017.

940  
941 Haeffelin M., Angelini F., et al: Evaluation of Mixing –Height Retrievals from Automatic Profiling  
942 Lidars and Ceilometers in View of Future Integrated Networks in Europe. *Boundary-layer Meteorol.*,  
943 143,49-75, 2012.

944  
945 Holben, B.N., Eck, T.F., Slutsker, I., Tanre, D., Buis, J.P., Setzer, A., Vermote, E., Reagan, J.A.,  
946 Kaufman, Y.J., Nakajima, T. and Lavenue, F.: AERONET—A federated instrument network and data  
947 archive for aerosol characterization. *Remote sensing of environment*, 66(1), 1-16, 1998.

948  
949 Hsu, N.C., Jeong, M.J., Bettenhausen, C., Sayer, A.M., Hansell, R., Seftor, C.S., Huang, J. and Tsay,  
950 S.C.: Enhanced Deep Blue aerosol retrieval algorithm: The second generation. *Journal of*  
951 *Geophysical Research: Atmospheres*, 118(16), 9296-9315, 2013.

970  
971 Jasim, F.H., Investigation of the 6-9 September 2015 Dust Storm over Middle East, *AJER*, 5 (11),  
972 201-207, 2016.

973  
974 Jolivet, D., Ramon, D., Bernard, E., Deschamps, P.Y., Riedi, J., Nicolas, J.M. and Hagolle, O.:  
975 Aerosol monitoring over land using MSG/SEVIRI. In *Proceeding of the EUMETSAT*  
976 *Meteorological Satellite Conference*, Darmstadt, Germany ,8-12, 2008.

977  
978 Kaskaoutis, D.G., Kambezidis, H.D., Nastos, P.T. and Kosmopoulos, P.G.: Study on an intense dust  
979 storm over Greece. *Atmospheric Environment*, 42(29), 6884-6896, 2008.

980

981 Koschmieder H.: Theorie der horizontalen sichtweite, Beitrage zur Physik der Freien Atmosphere  
982 12, 33–55,171–181, 1924.

983  
984  
985 Kotthaus, S., O'Connor, E., Munkel, C., Charlton-Perez, C., Gabey, A. M., and Grimmond, C. S. B.:  
986 Recommendations for processing atmospheric attenuated backscatter profiles from Vaisala CL31  
987 Ceilometers. *Atmos. Meas. Tech.*, 9, 3769-3791, 2016.

988  
989 Levi Y., Shilo E., Setter I.: Climatology of a summer coastal boundary layer with 1290-MHz wind  
990 profiler radar and a WRF simulation. *J. Appl. Meteo.*, 50(9), 1815-1826, 2011.

991  
992 Mamouri, R.E., Ansmann, A., Nisantzi, A., Solomos, S., Kallos, G. and Hadjimitsis, D.G.: Extreme  
993 dust storm over the eastern Mediterranean in September 2015: satellite, lidar, and surface  
994 observations in the Cyprus region, *Atmos. Chem. Phys.*, 16(21), 13711-13724, 2016.

995  
996 Mei, L., Xue, Y., de Leeuw, G., Holzer-Popp, T., Guang, J., Li, Y., Yang, L., Xu, H., Xu, X., Li, C.  
997 and Wang, Y.: Retrieval of aerosol optical depth over land based on a time series technique using  
998 MSG/SEVIRI data. *Atmospheric Chemistry and Physics*, 12(19), 9167–9185, 2012.

999  
1000 Mona, L., Liu, Z., Müller, D., Omar, A., Papayannis, A., Pappalardo, G., Sugimoto, N. and Vaughan,  
1001 M.: Lidar measurements for desert dust characterization: an overview. *Advances in*  
1002 *Meteorology*, 2012.

1003  
1004 Munkel C., Emeis S., Muller J. W., Schäfer K.: Aerosol concentration measurements with a lidar  
1005 ceilometer: results of a one year measuring campaign, *Remote sensing of Clouds and the*  
1006 *Atmosphere VIII*, 5235, 486-496, 2004.

1007  
1008 Munkel, C., Schäfer, K. and Emeis, S.: Adding confidence levels and error bars to mixing layer  
1009 heights detected by ceilometer, In *Proc. SPIE*, Vol. 8177, 817708-1, 2011.

1010  
1011 Papayannis, A., Amiridis, V., Mona, L., Tsaknakis, G., Balis, D., Bösenberg, J., Chaikovski, A., De  
1012 Tomasi, F., Grigorov, I., Mattis, I. and Mitev, V.: Systematic lidar observations of Saharan dust over  
1013 Europe in the frame of EARLINET (2000–2002). *Journal of Geophysical Research:*  
1014 *Atmospheres*, 113(D10), 2008.

1015  
1016  
1017  
1018  
1019  
1020  
1021  
1022  
1023  
1024  
1025  
1026  
1027  
1028  
1029  
1030  
1031  
1032  
1033  
1034  
1035  
1036  
1037  
1038  
1039  
1040  
1041  
1042  
1043  
1044  
1045  
1046  
1047  
1048  
1049

Parolari, A.J., Li, D., Bou-Zeid, E., Katul, G.G. and Assouline, S.: Climate, not conflict, explains extreme Middle East dust storm, *Environ. Res. Lett.*, 11, 114013, 2016.

Pu, B. and Ginoux, P.: The impact of the Pacific Decadal Oscillation on springtime dust activity in Syria, *Atmos. Chem. Phys.*, 16(21), 13431-13448, 2016.

Rao, P.G., Hatwar, H.R., Al-Sulaiti, M.H. and Al-Mulla, A.H.: Summer shamals over the Arabian Gulf. *Weather*, 58(12), 471-478, 2003.

Remer, L.A., Tanre, D., Kaufman, Y.J., Levy, R. and Mattoo, S.: Algorithm for remote sensing of tropospheric aerosol from MODIS: Collection 005. National Aeronautics and Space Administration, 1490, 2006.

Rieger, D., Bangert, M., Bischoff-Gauss, I., Förstner, J., Lundgren, K., Reinert, D., Schröter, J., Vogel, H., Zängl, G., Ruhnke, R. and Vogel, B.: ICON-ART 1.0-a new online-coupled model system from the global to regional scale. *Geosci. Model Dev.*, 8, 1659–1676, 2015

Roebeling, R. A., Feijt A. J., and Stammes P.: Cloud property retrievals for climate monitoring: Implications of differences between Spinning Enhanced Visible and Infrared Imager (SEVIRI) on METEOSAT-8 and Advanced Very High Resolution Radiometer (AVHRR) on NOAA-17, *J. Geophys. Res.*, 111(D20), 2006.

Romano, F., Ricciardelli, E., Cimini, D., Di Paola, F. and Viggiano, M.: Dust Detection and Optical Depth Retrieval Using MSG-SEVIRI Data. *Atmosphere*, 4(1), 35-47,2013.

[Scientific Validation Report SEVIRI Aerosol Optical Depth, EUMETSAT Satellite Application Facility on Climate Monitoring, 23 October 2017, doi: 10.5676/EUM\\_SAF\\_CM/MSG\\_AOD/V001.](#)

Solomos, S., Ansmann, A., Mamouri, R.-E., Biniotoglou, I., Patlakas, P., Marinou, E., and Amiridis, V.: Remote sensing and modeling analysis of the extreme dust storm hitting Middle East and Eastern Mediterranean in September 2015, *Atmos. Chem. Phys.*, 17, 4063-4079, 2017.

Stull R. B.: An introduction to boundary layer meteorology, Kluwer Academic publishers, Netherlands, 666p, 1988.



1050  
1051 Uzan L., Alpert P.: The coastal boundary layer and air pollution- A high temporal resolution analysis  
1052 in the East Mediterranean Coast, *The open atmospheric science journal*, 6 ,9-18, 2012.

1053  
1054 Uzan, L., Egert, S. and Alpert, P.: Ceilometer evaluation of the eastern Mediterranean summer  
1055 boundary layer height–first study of two Israeli sites. *Atmos. Meas. Tech.*, 9(9), 4387-4398, 2016.

1056  
1057 Vaisala ceilometer CL31 user's guide M210482EN-B, October, 2004.

1058  
1059 Wang, Y. Q.: *MeteoInfo: GIS software for meteorological data visualization and analysis. Met.*  
1060 *Apps*, 21, 360–368, 2014.

1061  
1062 Wiegner M. and Gasteiger J.: Correction of water vapor absorption for aerosol remote sensing with  
1063 ceilometers, *Atmos. Meas. Tech.*, 8, 3971–3984, 2015.

1064  
1065 Wiegner, M., Madonna, F., Biniotoglou, I., Forkel, R., Gasteiger, J., Geiß, A., Pappalardo, G., Schäfer,  
1066 K. and Thomas, W.: What is the benefit of ceilometers for aerosol remote sensing? An answer from  
1067 EARLINET, *Atmos. Meas. Tech.*, 7(7), 1979–1997, 2014.

1068  
1069 Winker, D.M., Vaughan, M.A., Omar, A., Hu, Y., Powell, K.A., Liu, Z., Hunt, W.H. and Young,  
1070 S.A.: Overview of the CALIPSO mission and CALIOP data processing algorithms. *Journal of*  
1071 *Atmospheric and Oceanic Technology*, 26(11), 2310-2323, 2009.

1084 Table 1. The publications on the September 2015 dust event

Publications	Title	Main Tool	Main outcome
Pu, B. and Ginoux, P (2016)	The impact of the Pacific Decadal Oscillation on springtime dust activity in Syria	MODIS Terra MODIS Aqua DOD AOD, GFDL-AM3 model	Model underestimation in the EM due to inaccurate soil moisture
Parolari et al. (2016)	Climate, not conflict, explains extreme Middle East dust storm	WRF model	Unusual low level westerly wind spread to the EM, to reversely transport the previously eastward particles back to the EM.
Mamouri et al. (2016)	Extreme dust storm over the eastern Mediterranean in September 2015: satellite, lidar, and surface observations in the Cyprus region	MODIS, EARLINET profiles and PM10	Dust plumes from Syria entered the EM in a double layer structure, pointing to multiple dust sources
<u>Stavros Solomos</u> et al. (2016)	Remote sensing and modeling analysis of the extreme dust storm hitting Middle East and Eastern Mediterranean in September 2015	RAMS model EARLINET lidar, MSG and CALIPSO.	Low model ability to simulate the event, due to inaccuracies in model physical processes.
Jasim, F.H. (2016)	Investigation of the 6-9 September 2015 Dust Storm over Middle East	Satellite MSG-SEVIRI, Meteoinfo model	Two dust storms simultaneously, from northern Syria and Sinai desert created by two low pressure systems
Gasch et al. (2017)	An analysis of the September 2015 severe dust event in the Eastern Mediterranean	ICON-ART model	An unusual early active Red Sea Trough with meso-scale convective systems generating cold-pool outflows producing the dust storm. Model lacked development of a super critical flow to produce excessive wind speeds

1085

1086

1087

1088

1089

1090

1091 Table 2. Ceilometers locations

Location	Site	Long/Lat	Distance from shoreline (km)	Height (m AGL)
Mount Meron	Northern	33.0/35.4	31	1,150
Ramat David	Northern	32.7/35.2	24	50
Hadera	Onshore	32.5/34.9	3.5	10
Tel Aviv	Onshore	32.1/34.8	0.05	5
Beit Dagan	Inland	32.0/34.8	7.5	33
Weizmann	Inland	31.9/34.8	11.5	60
Nevatim	Southern	31.2/34.9	44	400
Hazerim	Southern	31.2/34.7	70	200

1092 \*Ceilometer Weizmann is a CL51

1093

1094

1095

1096

1097 Table 3. Ceilometers configurations

Location	Type	Time resolution(sec)	Height resolution (m)	*Height range (km)
Mount Meron	CL31	16	10	7.7
Ramat David	CL31	16	10	7.7
Hadera	CL31	16	10	7.7
Tel Aviv	CL31	16	10	7.7
Beit Dagan	CL31	15	10	7.7
Weizmann	CL51	16	10	15.4
Nevatim	CL31	16	10	7.7
Hazerim	CL31	16	10	7.7

1098 \* Height range depends on sky conditions and is limited as AOD increases.

1099 \* In all ceilometers but in Beit Dagan site, data acquisition was limited to 4.5 km based on the BLview firmware

1100

1101

1102

1103

1104

1105

1106 Table 4. Ceilometer technical information

Location	Type	Engine board	Receiver	Transmitter	Firmware
Beit Dagan	CL31	CLE311	CLR311	CLT311	1.72
Weizmann	CL51	CLE321	CLRE321	CLT521	1.03

1107

1108

1109

1110

1111

1112 Table 5. Hourly maximum concentration of PM2.5, collected from 21 monitoring sites, between 7-10  
 1113 September 2015. The values are ranked from low (dark green) to high (dark red) values.

No.	Site	Height (m ASL)	Region	PM2.5 ( $\mu\text{g m}^{-3}$ )			
				7-Sep-15	8-Sep-15	9-Sep-15	10-Sep-15
1	Kefar Masarik	8	North	52	378	389	378
2	Ahuza	280	North	36	743	650	419
3	Newe Shaanan	240	North	43	400	466	525
4	Nesher	90	North	43	564	496	349
5	Kiryat Biyalic	25	North	53	424	703	447
6	Kiryat Binyamin	5	North	40	223	412	256
7	Kiryat Tivon	201	North	47	413	416	300
8	Afula	57	North	44	836	550	405
9	Raanana	54	Coast	38	173	291	229
10	Antolonsky	34	Coast	32	470	626	386
11	Ashdod	25	Coast	36	303	750	332
12	Ironi D	12	Coast	34	424	507	327
13	Tel aviv Central Station	29	Coast	41	716	803	451
14	Ashkelon	25	Coast	61	182	537	119
15	Jerusalem Efrata	749	Mountain	106	2285	434	403
16	Jerusalem Bar Ilan	770	Mountain	107	3063	641	518
17	Gedera	70	South	34	433	683	308
18	Nir Israel	30	South	25	363	638	228
19	Kiryat Gvaram	95	South	42	376	870	300
20	Sede Yoav	105	South	45	323	245	228
21	Negev Mizrahi	577	South	42	1748	526	317

1114  
 1115  
 1116  
 1117  
 1118  
 1119  
 1120  
 1121  
 1122  
 1123  
 1124  
 1125  
 1126  
 1127  
 1128  
 1129  
 1130  
 1131  
 1132

1133 Table 6. Hourly maximum concentration of PM10, collected from 31 monitoring sites, between 7-10  
 1134 September 2015. The values are ranked from low (dark green) to high (dark red) values.

No.	Site	Height (m ASL)	Region	PM10 ( $\mu\text{g m}^{-3}$ )			
				7-Sep-15	8-Sep-15	9-Sep-15	10-Sep-15
1	Galil Maaravi	297	North	114	3130	1987	1562
2	Karmelia	215	North	39	1120	1008	765
3	Newe Shaanan	240	North	104	3459	2471	1518
4	Haifa Port	0	North	78	1600	1965	1699
5	Nesher	90	North	117	3265	2746	1270
6	Kiryat Haim	0	North	82	1161	1625	1088
7	Afula	57	North	97	3239	2322	1961
8	Um El Kotof	0	Coast	99	2025	2028	1630
9	Orot Rabin	0	Coast	58	1152	1455	999
10	Barta	0	Coast	112	2540	2345	1612
11	Qysaria	19	Coast	54	1067	2116	1272
12	Rehuvot	70	Coast	88	2236	3045	1257
13	Givataim	0	Coast	112	1909	4014	1484
14	Yad Avner	77	Coast	61	1738	2902	1252
15	Aneil	20	Coast	96	2027	3472	1321
16	Shikun Lamed	17	Coast	51	1701	3244	1097
17	Station	29	Coast	87	1420	2176	998
18	Ashkelon	29	Coast	117	953	1692	551
19	Ariel	546	Mountain	128	2723	1481	1358
20	Jerusalem Efrata	770	Mountain	273	7820	1630	1437
21	Jerusalem Bar Ilan	749	Mountain	181	5588	1191	966
22	Jerusalem Safra	797	Mountain	491	10280	2389	1780
23	Gush Ezion	960	Mountain	310	6230	1679	1119
24	Erez	80	South	44	1000	1000	718
25	Beit Shemesh	350	South	115	2097	1943	1788
26	Caray Yosef	260	South	85	1047	784	594
27	Modiin	267	South	185	2701	2245	1980
28	Bat Hadar	54	South	65	1342	2563	841
29	Nir Galim	0	South	94	1479	2292	1027
30	Negev Mizrahi	577	South	183	9031	2806	1730
31	Eilat	0	South	275	1867	1592	1684

1135  
 1136  
 1137  
 1138  
 1139  
 1140  
 1141  
 1142